ARTICLE

Synaptic restoration by cAMP/PKA drives activity-dependent neuroprotection to motoneurons in ALS

Marcin Bączyk[1]*, Najwa Ouali Alami[2,8]*, Nicolas Delestrée[1]*, Clémence Martinot[1], Linyun Tang[2,3], Barbara Commisso[2,3], David Bayer[2,4], Nicolas Doisne[1], Wayne Frankel[5], Marin Manuel[1], Francesco Roselli[2,3,6,7]**, and Daniel Zytnicki[1]**

Excessive excitation is hypothesized to cause motoneuron (MN) degeneration in amyotrophic lateral sclerosis (ALS), but actual proof of hyperexcitation in vivo is missing, and trials based on this concept have failed. We demonstrate, by in vivo single-MN electrophysiology, that, contrary to expectations, excitatory responses evoked by sensory and brainstem inputs are reduced in MNs of presymptomatic mutSOD1 mice. This impairment correlates with disrupted postsynaptic clustering of Homer1b, Shank, and AMPAR subunits. Synaptic restoration can be achieved by activation of the cAMP/PKA pathway, by either intracellular injection of cAMP or DREADD-Gs stimulation. Furthermore, we reveal, through independent control of signaling and excitability allowed by multiplexed DREADD/PSAM chemogenetics, that PKA-induced restoration of synapses triggers an excitation-dependent decrease in misfolded SOD1 burden and autophagy overload. In turn, increased MN excitability contributes to restoring synaptic structures. Thus, the decrease of excitation to MN is an early but reversible event in ALS. Failure of the postsynaptic site, rather than hyperexcitation, drives disease pathobiochemistry.

Introduction

In amyotrophic lateral sclerosis (ALS), the "excitotoxic model" hypothesized that pathological increase in glutamatergic input at synaptic level and/or neuronal hyperexcitability would cause Ca^{2+} overload and disruption of mitochondria and ultimately lead to motoneuron (MN) death (Rothstein, 2009). In spinal muscular atrophy (SMA), a distinct MN disease, the reduced efficacy of the presynaptic terminals of Ia afferents (which originate from muscle spindles and provide direct, powerful excitation to MNs; Binder et al., 1993) disrupts MN firing (Mentis et al., 2011) and causes MN hyperexcitability (Fletcher et al., 2017). Likewise, in a *Drosophila* model of SMA, loss of the *Smn* gene in interneurons projecting to MNs is sufficient to cause MN degeneration (Imlach et al., 2012), confirming that disruption of synaptic inputs can drive MN vulnerability.

Interestingly, fast-fatigable MNs, the subpopulation most vulnerable in ALS, display the highest density of Ia afferents (Basaldella et al., 2015). Moreover, genetic ablation of gamma MNs (which likely reduces Ia firing) results in delayed disease onset, suggesting a detrimental effect of Ia activity (Lalancette-Hebert et al., 2016). However, degeneration of spindle sensory endings starts before symptom onset (Vaughan et al., 2015), rather suggesting that reduced Ia activity may be pathogenic. Furthermore, in contrast to SMA, vulnerable MNs in ALS become hypoexcitable just before the denervation onset of neuromuscular junctions (Martínez-Silva et al., 2018). Thus, if Ia fibers are involved in ALS as well, pathogenic and compensatory pathways may not necessarily be the same in the two conditions.

To date, direct in vivo proof of increased or decreased functionality of Ia synapses (and, more broadly, of any excitatory synapse) on MNs in presymptomatic ALS mice is lacking, and if it were so, it is unclear whether restoration of synaptic inputs may correlate with reduced disease burden. Here, we performed

[1]Université de Paris, Saints-Pères Paris Institute for the Neurosciences (SPPIN), Centre National de la Recherche Scientifique (CNRS), Paris, France; [2]Department of Neurology, Ulm University, Ulm, Germany; [3]Institute of Anatomy and Cell Biology, Ulm University, Ulm, Germany; [4]Cellular and Molecular Mechanisms in Aging Research Training Group, Ulm University, Ulm, Germany; [5]Department of Genetics & Development, Institute for Genomic Medicine, Columbia University Irving Medical Center, New York, NY; [6]German Center for Neurodegenerative Diseases, Ulm, Germany; [7]Neurozentrum Ulm, Ulm, Germany; [8]International Graduate School in Molecular Medicine Ulm, Ulm University, Ulm, Germany.

*M. Bączyk and N. Ouali Alami contributed equally to this paper; **F. Roselli and D. Zytnicki contributed equally to this paper; Correspondence to Daniel Zytnicki: daniel.zytnicki@parisdescartes.fr; Francesco Roselli: francesco.roselli@uni-ulm.de; M. Bączyk's present address is Department of Neurobiology, Poznań University of Physical Education, Poznan, Poland; N. Ouali Alami's present address is Department of Neurology, Clinical Neuroanatomy, Ulm University, Ulm, Germany; N. Delestrée's present address is Department of Pathology and Cell Biology, Columbia University, New York, NY.

Check for updates

in vivo electrophysiological recordings to demonstrate that MN response to Ia synapses is actually disrupted in presymptomatic mutant superoxide dismutase 1 (mutSOD1) mice, in correlation with the breakdown of the postsynaptic receptor clusters and scaffold proteins. We then used multiplexed chemogenetics to show that synaptic impairment could be acutely and chronically reversed by activation of the cAMP/protein kinase A (PKA) pathway in MNs, with activity-dependent beneficial effects on disease burden. Moreover, we show that functional and structural synaptic impairment is detected also in monosynaptic excitatory postsynaptic potentials (EPSPs) on MNs from the descending medial longitudinal fasciculus (MLF). Thus, our work shows that dysfunction of excitatory synapses, largely of postsynaptic origin, reduces the excitatory drive to MNs and may contribute to MN degeneration in ALS through decreased MN firing.

Results

The monosynaptic excitatory pathway between Ia afferents and MNs is impaired in presymptomatic SOD1(G93A) mice

We investigated the Ia synaptic responses in MNs, in vivo, in 45–55-d-old anesthetized SOD1(G93A) mice (hereafter, mutSOD1), before fast-fatigable MN denervation (Pun et al., 2006). We activated the spindle primary endings in vivo using high-frequency vibrations of the Achilles tendon while intracellularly recording the EPSP elicited in a triceps surae (TS) MN (Fig. 1 A). The vibration-induced compound EPSPs (resulting from the summation of one EPSP per vibration cycle, insert in Fig. 1 B_2) were on average 30% smaller in MNs from mutant mutSOD1 animals than in MNs from animals expressing the human WT SOD1 protein (wtSOD1; Fig. 1, B and C).

Because the reduction of the EPSPs induced by tendon vibration could be caused by disruption of the spindles themselves, we bypassed the spindles by recording the monosynaptic EPSPs elicited by a direct electrical stimulation of Ia afferents in the TS nerve (Fig. 1 D) at an intensity that recruits all group I fibers (1.8–2.0× threshold of the most excitable afferents). At this intensity (and up to 5× threshold), no disynaptic EPSPs were visible, and disynaptic inhibitory postsynaptic potentials, if present, appeared only after the peak of the monosynaptic EPSP where measurements were made (Fig. S1, A–C). The EPSPs elicited by a single electrical shock (no summation) were again, on average, 33% smaller in MNs from mutSOD1 animals than in MNs from wtSOD1 animals (Fig. 1, E and F), indicating that the reduction was not due to spindle impairments. Input resistances (Fig. 1 G), membrane time constants (Fig. 1 H), and resting membrane potentials (Fig. 1 I) were all comparable between wtSOD1 and mutSOD1 animals, ruling out additional confounders and establishing that the impairment originates in the synapses themselves.

Because activation of presynaptic axo-axonic GABAergic synapses may reduce the size of the EPSPs (Rudomin and Schmidt, 1999), we investigated whether presynaptic inhibition of Ia terminals is stronger in mutSOD1 than in wtSOD1 mice. As in cats (Rudomin and Schmidt, 1999), mouse group I fibers from the posterior biceps elicit some presynaptic inhibition of Ia afferents from the TS (Fig. S1, D–G). However, the level of presynaptic inhibition

was not significantly different between mutSOD1 and wtSOD1 mice (Fig. S1 H). Therefore, the reduction in the size of EPSPs in mutSOD1 MNs cannot be explained by an increase of presynaptic inhibition of Ia terminals. We then studied the paired-pulse facilitation of Ia synapses on MNs. In wtSOD1 mice, the second Ia EPSP evoked by paired-pulse stimulation was systematically larger than the first one (paired-pulse facilitation; Fig. 1, J–L), a finding compatible with the contribution of presynaptic inhibition (Stuart and Redman, 1991; Carlsen and Perrier, 2014). However, in mutSOD1 mice, many MNs displayed a paired-pulse ratio of reduced magnitude, with half of the MNs actually displaying a net paired-pulse depression (Fig. 1, K and L), despite that the level of presynaptic inhibition was the same as in wtSOD1 mice (Fig. S1 H). This suggests that the SOD1 mutation elicits a depressing effect on the second EPSP that sometimes surpasses the facilitation generated by presynaptic inhibition. In summary, we show that, in mutSOD1 mice, Ia-MN synapses display abnormal physiological properties in terms of not only evoked EPSP, but also short-term synaptic plasticity.
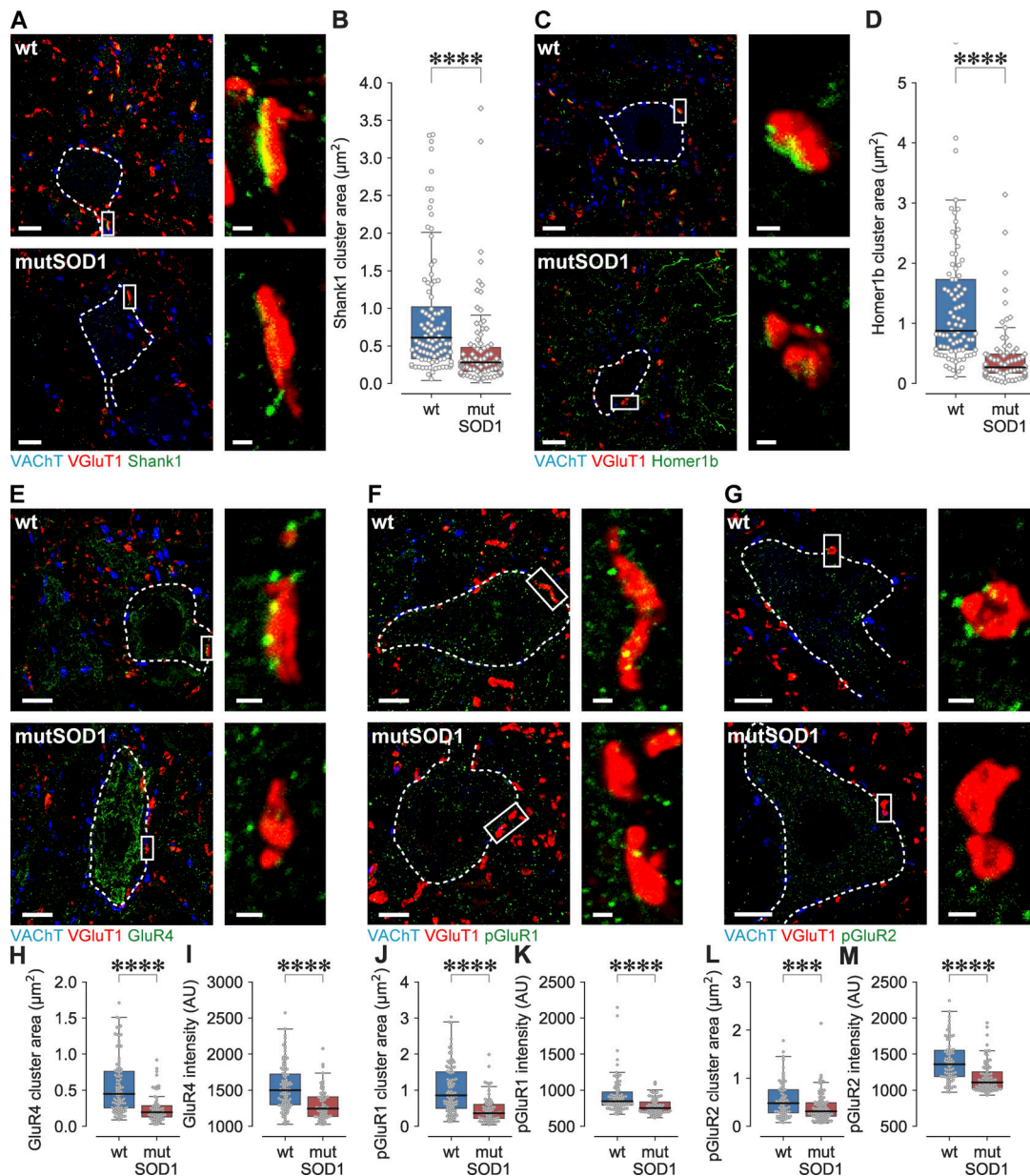
The postsynaptic side of Ia synapses on MNs is structurally disrupted in mutant mice

We investigated the origin of synaptic dysfunction using immunolabeling of pre- and postsynaptic proteins. Ia boutons onto MNs were identified by the expression of vesicular glutamate transporter 1 (VGluT1; Alvarez et al., 2011). Because VGluT1+ synapse density is higher close to the soma and decreases with distance (Rotterman et al., 2014), we first estimated the density of VGluT1+ terminals separately on cell bodies, proximal dendrites, and distal dendrites of intracellularly labeled MNs (Fig. S2, A and B). Density of VGluT1+ terminals in these three compartments was unchanged in mutSOD1 mice (Fig. S2, C and D). These data indicate that the smaller EPSP size in mutant mice is not due to a reduced number of Ia boutons. Moreover, we confirmed the integrity of the Ia presynaptic terminals by immunolabeling (Fig. S2, E and F). Size and immunostaining intensity of VGluT1+ boutons (Fig. S2, G and H) were comparable in WT and mutSOD1 mice. Likewise, the fluorescence intensity and size of the clusters of synaptophysin (Fig. S2, I and J) and bassoon (Fig. S2, K and L) contained in VGluT1+ terminals were normal in mutSOD1 mice. Taken together, these data indicate that the smaller EPSP size in mutant mice is due to neither a reduced number of Ia boutons nor their structural disturbance.

We then focused on the postsynaptic side of the VGluT1+ synapses on MNs. We first analyzed the expression of the postsynaptic density (PSD) proteins Shank1 and Homer1b (Fig. 2, A–D), critical organizers of the PSD (Sheng and Hoogenraad, 2007). In WT MNs, both Shank1 and Homer1b formed large, continuous clusters juxtaposed and parallel to the VGluT1+ puncta. However, in mutSOD1 mice, VGluT1+ synapses displayed smaller and fragmented clusters of Shank1 (Fig. 2, A and B) and Homer1b (Fig. 2, C and D). We then explored the distribution of α-amino-3-hydroxy-5-methyl-4-isoxazolepropionic acid (AMPA) receptor subunit GluR4, the most abundant subunit expressed in MNs (Williams et al., 1996; Ragnarson et al., 2003), at VGluT1+ synapses. In WT MNs, GluR4 formed multiple, discrete, and round clusters juxtaposed to each VGluT1+ puncta (Fig. 2 E). MutSOD1
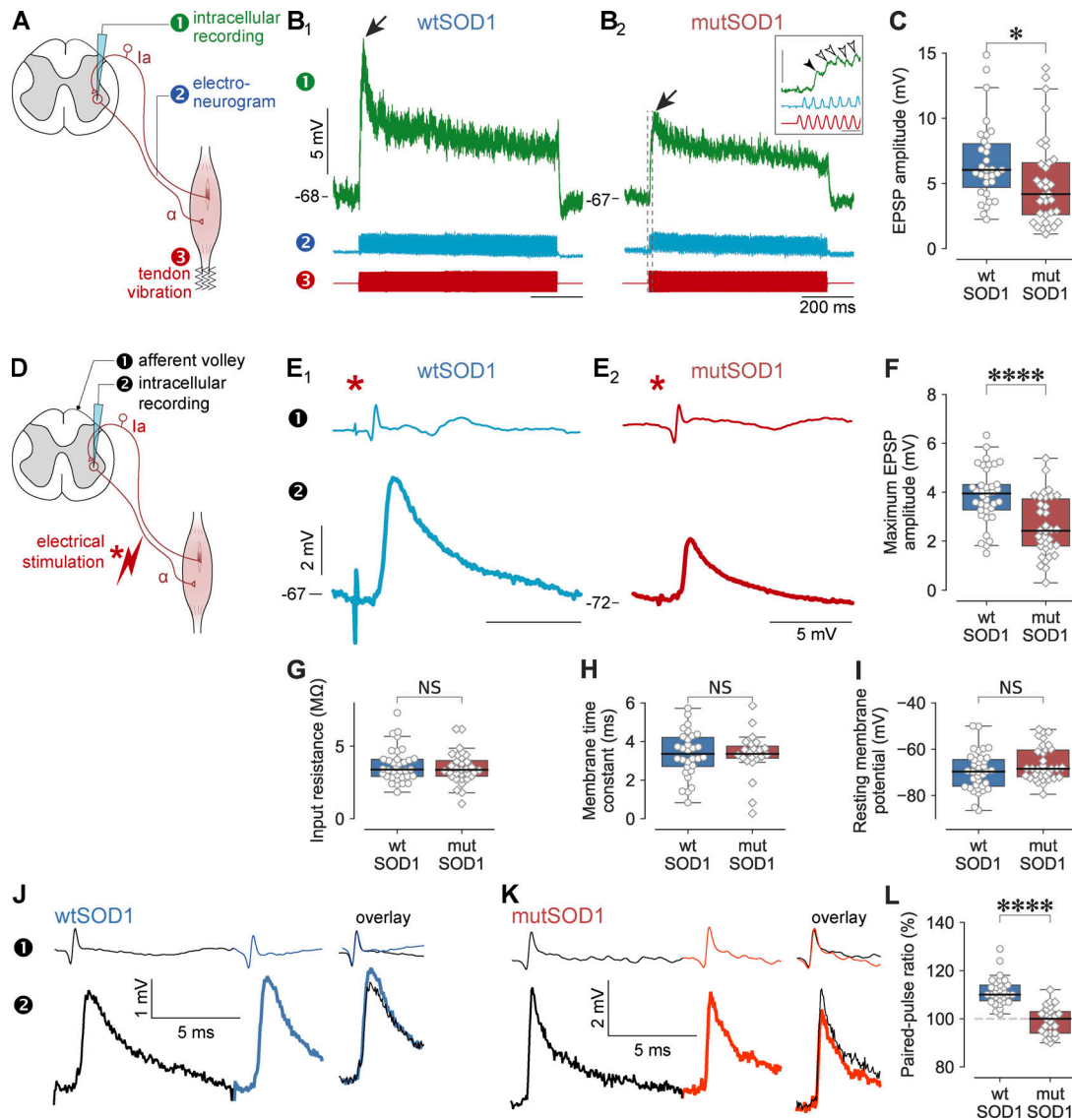
Figure 1. **Monosynaptic Ia EPSPs are smaller in mutant mice. (A)** Stimulation and recording arrangement for tendon vibrations (450 Hz) of TS. **(B)** Responses in a wtSOD1 (B₁) and a mutSOD1 (B₂) MN. (1) Membrane potential; (2) ENG recording showing the response of the Ia sensory afferents to the vibration; and (3) vibration. Arrows on the voltage traces indicate the peak deflection at which EPSP amplitude was measured (the subsequent sag is most likely caused by a deactivation of the Ih current; Manuel et al., 2007). The insert is an expansion between the vertical dashed lines showing the modulations of the ENG (which reflect the activity of Ia afferents; blue trace) and the EPSP summation (green trace) upon the repetition of vibrations (vertical bar, 5 mV; horizontal bar, 5 ms). A summation of the EPSPs elicited by the successive vibrations occurs because the vibration period (2.5 ms) is shorter than the single EPSP duration: the EPSP elicited by the first vibration (filled arrowhead in the insert) is smaller than the EPSPs elicited by the subsequent vibrations (unfilled arrowheads). **(C)** Comparison of EPSP amplitudes from wtSOD1 (7.3 ± 4.7 mV, $n = 32$, seven mice) and mutSOD1 mice (5.1 ± 3.5 mV, $n = 33$, eight mice). MW, *, $P = 0.015$. **(D)** Stimulation and recording arrangement for TS nerve stimulations. **(E)** Representative traces of the maximal group I volley (top trace, [1]) and EPSP (bottom trace, [2]) recorded in a wtSOD1 (E₁) and a mutSOD1 MN (E₂). Red asterisks above the volley indicate the stimulation time. **(F)** Comparison of the maximal electrically evoked EPSP in wtSOD1 (3.9 ± 1.1 mV, $n = 37$, seven mice) and mutSOD1 animals (2.6 ± 1.2 mV, $n = 34$, nine mice), t test, ****, $P < 0.0001$. **(G)** Peak input resistance (wtSOD1: 3.7 ± 1.2 MΩ, $n = 35$; vs. mutSOD1: 3.5 ± 1.1 MΩ, $n = 32$, MW, $P = 0.768$). **(H)** Membrane time constant (wtSOD1: 3.4 ± 1.2 ms, $n = 30$; vs. mutSOD1: 3.3 ± 1.2 ms, $n = 23$, MW, $P = 1.0$). **(I)** Resting potential (wtSOD1: −69.6 ± 8.3 mV, $n = 36$; vs. mutSOD1: −66.4 ± 7.5 mV, $n = 34$, MW, $P = 0.32$). These properties were also not different in the MN sample tested with tendon vibration (not depicted); peak input resistance: wtSOD1: 3.8 ± 1.8 MΩ, $n = 31$; vs. mutSOD1: 3.5 ± 1.4 MΩ, $n = 33$, MW, $P = 0.55$; membrane time constant: wtSOD1: 3.2 ± 1.4 ms, $n = 29$; vs. mutSOD1: 3.4 ± 1.2 ms, $n = 33$, MW, $P = 0.37$; resting membrane potential: wtSOD1: −65.9 ± 10.3 mV, $n = 32$; vs. mutSOD1: −67.7 ± 10.3 mV, $n = 33$; MW, $P = 0.50$. **(J and K)** Afferent volleys (top traces) and EPSPs (bottom traces) recorded from triceps MNs evoked by two group I stimulations separated by 10-ms intervals. The stimulation intensity was adjusted to obtain submaximal EPSP amplitude. Overlay: Superimposed first and second volleys and EPSPs (black thin line, first EPSP; thicker colored trace, second EPSP). EPSP changes were not related to afferent volley fluctuations (see top traces) and were therefore caused by synaptic plasticity. **(L)** Comparison of the paired-pulse ratios (PPRs) of second versus first EPSP for wtSOD1 and mutant mice. For 12 of 25 mutSOD1 MNs, the paired-pulse stimulation resulted in a depression (<100%). Such a depression was not seen in wtSOD1 MNs. On average, the PPR was significantly smaller in MNs from mutant animals (0.99 ± 0.06, $n = 25$, from eight mice) compared with MNs from controls (1.11 ± 0.06, $n = 31$, from seven mice, MW, ****, $P < 0.0001$). Note that the EPSP decay time constant (measured on the first EPSP) was not different in mutSOD1 MNs (2.7 ± 1.0 ms, $n = 25$) compared with wtSOD1 MNs (2.6 ± 1.5 ms, $n = 31$, MW, $P = 0.35$; not depicted). All records were obtained with the Na⁺ channel blocker QX-314 in the microelectrode intracellular solution to prevent spiking. In all graphs, each point represents one MN.

Figure 2. **Alterations in the postsynaptic structure of VGluT1+ synapses onto MNs. (A and B)** The size of Shank1 clusters juxtaposed to VGluT1+ terminals on MNs is significantly reduced in mutSOD1 MNs (WT: 0.92 ± 0.96 μm², n = 164; vs. mutSOD1: 0.48 ± 0.62 μm², n = 149; MW, ****, P < 0.0001). **(C and D)** Homer1b clusters juxtaposed to VGluT1+ synapses are significantly smaller in mutSOD1 (WT: 1.35 ± 1.31 μm², n = 86; vs. mutSOD1: 0.43 ± 0.52 μm², n = 78; MW, ****, P < 0.0001). **(E–G)** Representative images showing the GluR4 (E), phospho-GluR1 (F), and phospho-GluR2 (G) clusters at VGluT1+ synapses in WT and mutSOD1 MNs. **(H and I)** Significant reduction in GluR4 cluster area (WT: 0.56 ± 0.39 μm², n = 99; vs. mutSOD1: 0.25 ± 0.20 μm², n = 64; MW, ****, P < 0.0001) and fluorescence intensity (WT: 1542 ± 319, n = 99 vs. mutSOD1: 1300 ± 220, n = 64; MW, ****, P < 0.0001) in mutSOD1 mice. **(J and K)** Significant decrease in pGluR1 cluster area (WT: 1.04 ± 0.68 μm², n = 132; vs. mutSOD1: 0.45 ± 0.34 μm², n = 96; MW, ****, P < 0.0001) and fluorescence intensity (WT: 915 ± 218, n = 132; vs. mutSOD1: 785 ± 122, n = 96; MW, ****, P < 0.0001) in mutSOD1 mice. **(L and M)** Significant decrease in pGluR2 cluster area (WT: 0.55 ± 0.37 μm², n = 89; vs. mutSOD1: 0.39 ± 0.29 μm², n = 109; MW, ***, P = 0.0004) and fluorescence intensity (WT: 1401 ± 281, n = 89; vs. mutSOD1: 1173 ± 198, n = 109; MW, ****, P < 0.0001) in mutSOD1 mice. Each data point represents a single synapse. In all panels, the dotted line represents the approximate outline of the MNs. Scale bars: 10 μm (insert: 1 μm). The experiment was conducted on three WT and three mutSOD1 mice at P40.

MNs, on the other hand, displayed a significant decrease in the total GluR4 cluster area (Fig. 2 H) and in their immunostaining intensity (Fig. 2 I). We further explored the disruption of the postsynaptic structures by assessing the level of T840-phosphorylated GluR1 (Fig. 2 F), whose levels reflect AMPAR with increased conductance (Delgado et al., 2007; Jenkins et al., 2014; Babiec et al., 2016), and S880-phosphorylated GluR2 (Fig. 2 G), a marker of GluR2 subunits

stably retained in synapses (States et al., 2008). The size and fluorescence intensity of both pGluR1 and pGluR2 clusters juxtaposed to VGluT1+ terminals were significantly decreased in mutSOD1 mice (Fig. 2, J–M). Taken together, these data show a significant disruption of the structure of the PSD of VGluT1+ synapses and support the view of a substantial postsynaptic component in driving the physiological disturbance of MN responses to Ia afferents.

We further investigated whether the disruption of Ia PSDs could be associated with other structural abnormalities. We exploited neurobiotin ability to fill the dendrite cytoplasm of the neurons, negatively highlighting intraneuronal dendritic structures. This approach revealed large vacuoles located in the varicosities along dendritic branches (Fig. S3). In addition, many VGluT1+ synapses were located in close apposition to these vacuoles (Fig. S2 B). Vacuoles were already visible around postnatal day 50 (P50) in mutSOD1 mice (Fig. S3 C) but not in WT and in wtSOD1 mice (Fig. S3, A and B) and imparted a significant distortion in the geometry of the dendrite. The size of the vacuoles and their impact on dendritic architectures increased with disease progression (Fig. S3 C). Thus, substantial structural disruption of dendritic architecture takes place in close proximity of VGluT1+ synapses already at early stages and increases with disease progression.

Postsynaptic activation of the PKA pathway elicits a partial functional rescue of the Ia-MN synapses

Next, we reasoned that reduced EPSP size might be ameliorated by increasing the insertion of AMPA receptors in the postsynaptic membrane. Because phosphorylation of GluR4 by PKA on Ser842 is sufficient to relieve a retention signal in the C-terminus and allows its synaptic insertion (Esteban et al., 2003), we explored whether activation of PKA in MNs might restore Ia-MN EPSP size. We applied the PKA activator cAMPS-Sp by intracellular iontophoretic injection through the recording microelectrode (Lalley et al., 1997) while recording electrically evoked Ia EPSPs before and after injection. In mutSOD1 MNs, PKA activation resulted in the progressive increase of EPSP size in all MNs tested (Fig. 3, A_2 and C_2; 14% on average, i.e., about half of the average EPSP size reduction in the mutSOD1 animals). This restoration took place in the first 5 min and remained stable over the duration of the recording session (which may have lasted 20 min). Furthermore, iontophoretic injection of cAMPS-Sp also partially restored the paired-pulse facilitation (Fig. 3, B_2 and D_2). On the other hand, the stimulation protocol alone (without cAMPS-Sp injection) did not modify EPSP size in three independent MNs. In contrast, in wtSOD1 mice, cAMPS-Sp induced only a small increase of EPSP size (7% on average; Fig. 3, A_1 and C_1) but had no significant effect on the paired-pulse ratio (Fig. 3, B_1 and D_1). These results not only further confirm that the functional impairment of the Ia-MN synapses has a major postsynaptic origin, but also show that it is acutely reversible. Furthermore, since the cAMPS-Sp was applied postsynaptically, these results confirm a major role of postsynaptic mechanisms in the origin of depressed paired-pulse response of mutSOD1 MNs.

### Chemogenetic activation of PKA pathway in MNs enhances GluR4 content and Homer1b in Ia synapses

Because iontophoretic delivery allows the study of the effects of PKA activation for only ~20 min (limited by the stability of the preparation), we sought to manipulate the cAMP/PKA pathway over hours/days through the use of a Gs-coupled designer receptor exclusively activated by designer drugs (DREADD; Farrell et al., 2013; Aldrin-Kirk et al., 2016; Roth, 2016). To this aim, 25-d-old mutSOD1/choline acetyltransferase (ChAT)-cre double-

transgenic mice were intraspinally injected with AAV9 encoding for double-floxed DREADD(Gs)-mCherry (henceforth D(Gs)); thus, D(Gs) expression was restricted to ChAT-cre+ cells. A first group of mice was administered a single dose of clozapine-N-oxide (CNO) 17 d after the viral injection (acute CNO; Fig. 3 E_2) and sacrificed 3 h later; a second group was administered CNO daily starting 10 d after virus injection and for 7 d (chronic CNO; Fig. 3 E_3) and sacrificed 8 h after the last injection (thus, 17 d after viral injection); and a third group was treated only with saline for 7 d (control group; Fig. 3 E_1). For each mouse, we quantified GluR4 and Homer1b cluster area in VGluT1+ synapses on MNs expressing D(Gs) (mCherry+) as well as on contralateral noninfected (mCherry−) MNs. Extending the intracellular injection data, acute (3-h) activation of D(Gs) resulted in the significant increase in GluR4 (Fig. 3, F_2 and H) as well as Homer1b cluster area (Fig. 3, G_2 and I) in VGluT1+ terminals. Long-term (7-d) activation of D(Gs) also resulted in a significant restoration of GluR4 (Fig. 3, F_3 and H) and Homer1b cluster area in Ia synapses (Fig. 3, G_3 and I) compared with contralateral MNs (which were exposed to the same dose of CNO but did not express any chemogenetic receptor). No effect on GluR4 (Fig. 3, F_1 and H) or Homer1b (Fig. 3, G_1 and I) was detected in mice expressing D(Gs) but administered with vehicle alone compared with contralateral noninfected MNs, indicating that intraspinal injection and D(Gs) expression did not produce any substantial effect. Thus, cAMP/PKA activation is sufficient to restore the structure and the function of Ia synapses, increasing GluR4 and Homer1b content in the postsynaptic side.

PKA effects on the postsynaptic side of Ia terminals do not require MN firing but are mimicked by chemogenetic excitation of MNs

Hypoexcitability of vulnerable MNs is an early event in the pathogenic cascades leading to MN degeneration (Martínez-Silva et al., 2018), and restoration of MN firing produces beneficial effects on multiple disease markers (Saxena et al., 2013). Therefore, we set out to verify whether synaptic restoration could be also obtained by enhancing MN firing with chemogenetic cation-permeable (activator pharmacologically selective actuator module [actPSAM]; Magnus et al., 2011; Saxena et al., 2013). AAV9 encoding for actPSAM under double-inverted orientation was injected intraspinally in mutSOD1/ChAT-cre mice at P25. The PSAM agonist pharmacologically selective effector molecule 308 (PSEM[308]) was then administered 10 d later for 7 d (Fig. S4 B). Compared with contralateral noninfected MNs, PSAM-activated MNs displayed a significant increase in both GluR4 and Homer1b cluster area in correspondence to VGluT1+ synapses (Fig. S4, C–F).

We then wondered whether the effect of cAMP/PKA on synapses could be due to an effect on MN firing. To test this hypothesis, we designed a multiplexed chemogenetic experiment in which PKA signaling and MN firing could be independently controlled. We coinjected an AAV9 encoding D(Gs)-mCherry together with a second AAV9 encoding inhPSAM, the anion-permeable (inactivator) PSAM–glycine receptor (GlyR; Magnus et al., 2011), both under double-floxed inverted orientation, in the spinal cord of mutSOD1/ChAT-cre mice (Fig. 4 A). We reasoned that if the effect of cAMP/PKA on synaptic
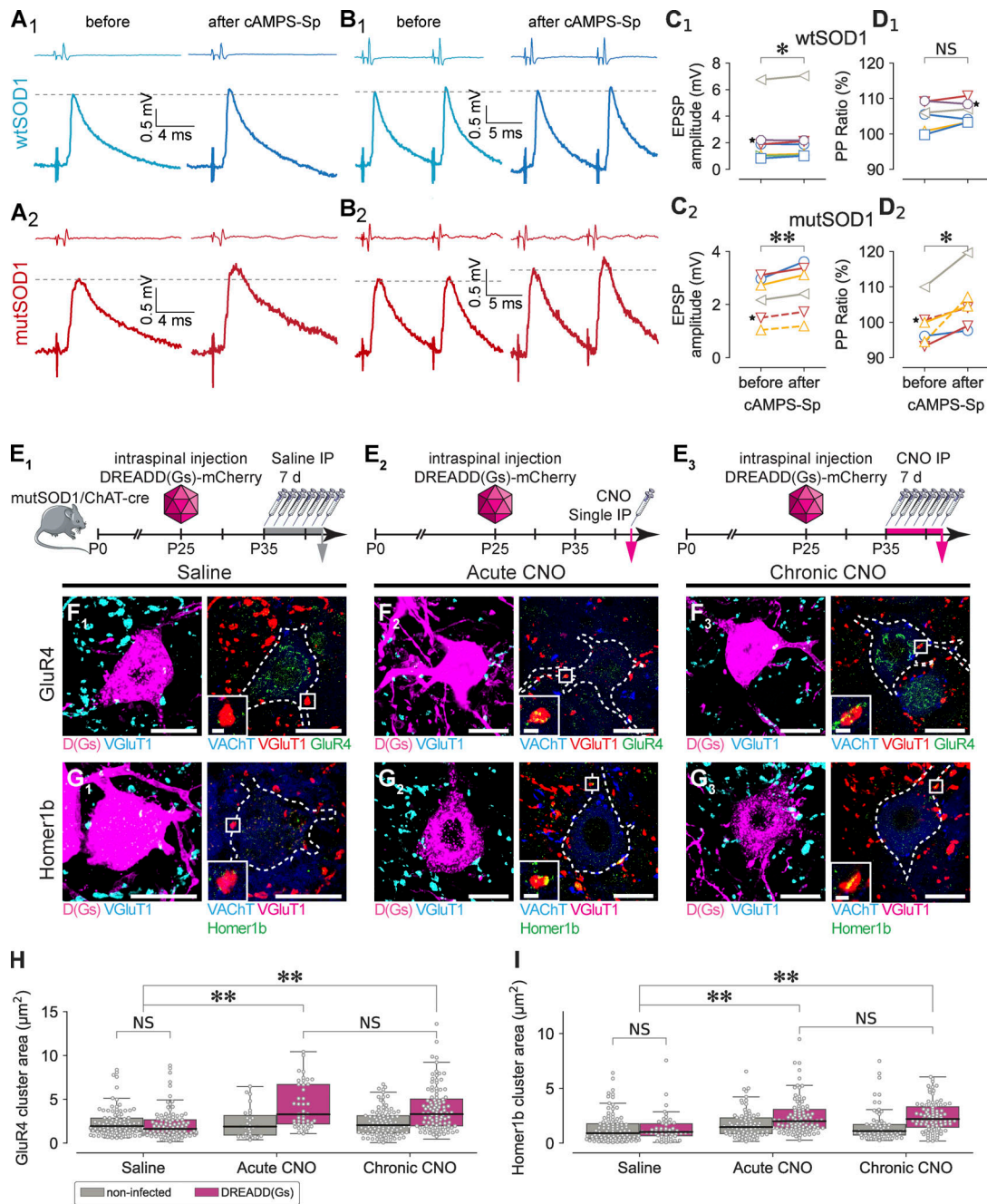
Figure 3. **Postsynaptic activation of the PKA pathway enhances Ia EPSPs and restores synaptic structures. (A)** Effect of iontophoretic injection of cAMPS-Sp on Ia EPSP amplitude. Afferent volleys (top traces) and EPSPs in TS MNs (bottom traces) evoked by electrical stimulation of the TS nerve recorded immediately before and a few minutes after the injection of the compound. **(B)** Effect of iontophoretic injection of cAMPS-Sp on paired-pulse ratios. Same MNs and same time points as in A. **(C)** Quantification of the increase in EPSP size. "Before" values were measured just before the injection; "after" values are averages over the whole duration of the recording after the injection. Each symbol represents one MN, and the stars next to the symbols represent the MNs shown in A. **(C1)** In wtSOD1 animals (four mice), cAMPS-Sp increased the size of the EPSPs by 7 ± 8%; $n = 7$; paired t test, *, P = 0.04. **(C2)** In mutSOD1 animals (two mice), the EPSP size increased by 14 ± 5% on average, $n = 6$; paired t test, **, P = 0.007. In mutant animals, the experiments were conducted in four MNs: Ia EPSPs coming from either of the two TS branches were tested in two MNs, whereas only one source of Ia excitation was tested in the remaining two MNs (see different symbols and line styles in C2). The difference persists if we consider only EPSPs elicited by stimulation of the LG nerve in each MN. The EPSP size increased by 14 ± 6% on average, $n = 4$; paired t test, P = 0.02. **(D)** Quantification of the change in the paired-pulse ratio after cAMPS-Sp injection. Same organization as in C. In wtSOD1 animals (four mice), cAMPS-Sp did not significantly change the paired-pulse ratio (D1, average difference 1 ± 2%; $n = 6$, paired t test, P = 0.23), while it caused an increase by 5 ± 5%, $n = 6$ in mutSOD1 animals (D2, two mice, paired-pulse ratio before, 1.00 ± 0.06, $n = 6$; vs. after, 1.05 ± 0.08, $n = 6$; paired t test, *, P = 0.038). As before, the difference persists if we consider only EPSPs elicited by the LG nerve in each MN. cAMPS-Sp increased the paired-pulse ratio from 1.00 ± 0.07 to 1.05 ± 0.10, $n = 4$; paired t test, P = 0.048. **(E)** Experimental design for DREADD experiments. **(F)** MNs expressing D(Gs) and immunostained for VGluT1 and GluR4 under either vehicle (F1), acute CNO (F2), or chronic CNO treatment (F3). The dotted line represents the approximate outline of the MNs. MNs are identified by VAChT staining. Scale bars: 20 μm (inset: 1 μm). **(G)** Same organization as F, but immunostained for VGluT1 and Homer1b. **(H)** Significant increase in GluR4 cluster area in VGlut1 synapses of D(Gs)+ MNs (magenta) compared with contralateral D(Gs)− MNs (gray) upon acute

(4.3 ± 2.6 μm^2, n = 43; vs. 2.3 ± 1.7 μm^2, n = 27; from three mice; two-way ANOVA followed by Tukey HSD, **, P = 0.001) and chronic (3.9 ± 2.5 μm^2, n = 144; vs. 2.3 ± 1.5 μm^2, n = 128; from four mice; Tukey HSD, **, P = 0.001) CNO treatment, but not in vehicle-treated mice (2.1 ± 1.6 μm^2, n = 119; vs. 2.3 ± 1.6 μm^2, n = 111; from three mice; Tukey HSD, P = 0.9). **(I)** Significant increase in Homer1b cluster area in D(Gs)$^+$ MNs compared with contralateral D(Gs)$^-$ MNs upon acute (2.4 ± 1.6 μm^2, n = 109; vs. 1.8 ± 1.2 μm^2, n = 83; two-way ANOVA followed by Tukey HSD, **, P = 0.0147) and chronic (2.4 ± 1.5, n = 88; vs. 1.6 ± 1.4 μm^2, n = 69; from four mice; Tukey HSD, **, P = 0.0019) CNO treatment, but not in vehicle-treated mice (1.4 ± 1.2 μm^2 in D(Gs)$^+$ MNs, n = 51; vs. 1.3 ± 1.6 μm^2 in D(Gs)$^-$ MNs, n = 117; from three mice; Tukey HSD, P = 0.9).

integrity is secondary to changes in MN activity, it would be significantly decreased upon concomitant decrease in MN firing. 10 d after AAV injection, we started the administration of CNO and PSEM[308] for 7 d (Fig. 4 A). We considered four populations of MNs: (i) contralateral, noninfected; (ii) expressing only the inhPSAM; (iii) expressing only D(Gs); and (iv) expressing both D(Gs) and inhPSAM. We also quantified GluR4 (Fig. 4, B and D) and Homer1b (Fig. 4, C and E) levels in VGluT1$^+$ synapses.

Compared with noninfected MNs, inactivation of MNs by inhPSAM did not result in a further decrease in the already low levels of GluR4 (Fig. 4 D) or Homer1b (Fig. 4 E), which would have been anticipated, since MN inactivation worsens disease progression (Saxena et al., 2013; a small increase in GluR4 content in Ia synapses was detected). As shown above, D(Gs) activation alone did result in a significant increase of synaptic GluR4 and Homer1b cluster area (Fig. 4, D and E). However,
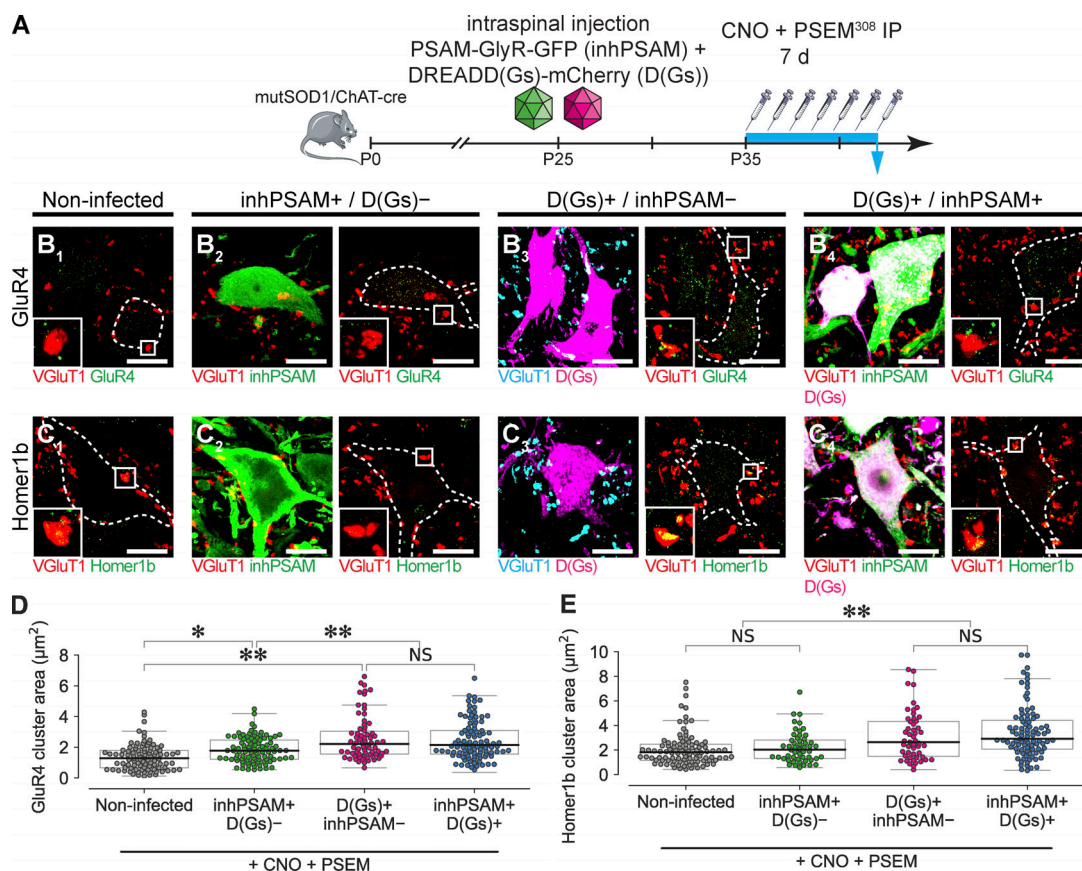
Figure 4. **PKA effects on the postsynaptic side of Ia terminals do not depend on MN intrinsic excitation. (A)** Experimental design for the double-chemogenetics control of MN excitation (by PSAM-GlyR-GFP, for brevity inhPSAM) and PKA signaling (by D(Gs)-mCherry) on synaptic GluR4 and Homer1b levels. **(B)** Uninfected MN (inhPSAM$^-$/D(Gs)$^-$; B$_1$), MNs expressing either inhPSAM only (inhPSAM$^+$/D(Gs)$^-$, green; B$_2$), D(Gs) only (D(Gs)$^+$/inhPSAM$^-$, magenta; B$_3$), or both (D(Gs)$^+$/inhPSAM$^+$, white; B$_4$) and immunostained for VGluT1 and GluR4. **(C)** Representative images of uninfected MN (C$_1$) or expressing either inhPSAM only (green; C$_2$) or D(Gs) only (magenta; C$_3$) or both (white; C$_4$) and immunostained for VGluT1 and Homer1b. The outline of each MN is marked by the dashed line. Scale bars: 20 μm (inset: 1 μm). **(D)** Activation of inhPSAM causes only a minor increase in GluR4 cluster area compared with noninfected MNs (1.84 ± 0.81, n = 97; vs. 1.35 ± 0.84 μm^2, n = 95; one-way ANOVA followed by Tukey HSD, *, P = 0.02) whereas D(Gs) activation enhances GluR4 cluster area in VGluT1$^+$ synapses (2.59 ± 1.45 μm^2; n = 70; Tukey HSD, **, P = 0.001 compared with noninfected MNs, and P = 0.001 compared with inhPSAM$^+$/D(Gs)$^-$ MNs). The concomitant inactivation of MNs by inhPSAM and the activation of D(Gs) did not reduce the effect of D(Gs) (2.45 ± 1.30 μm^2; n = 175; Tukey HSD, P = 0.80 vs. D(Gs)$^+$/inhPSAM$^-$ MNs). **(E)** D(Gs) activation increased the size of Homer1b clusters (3.14 ± 2.01 μm^2; n = 51) compared with noninfected MNs (2.10 ± 1.41 μm^2; n = 106; ANOVA followed by Tukey HSD, **, P = 0.003). Notably, inhPSAM by itself did not have any effect on Homer1b cluster area (2.23 ± 1.27 μm^2; n = 52; Tukey HSD, P = 0.9) and did not diminish the effect of D(Gs) activation (3.46 ± 2.12 μm^2; n = 91; Tukey HSD, P = 0.68). This experiment was conducted on five mutSOD1/ChAT-cre mice.

D(Gs) effects on GluR4 and Homer1b were not modified by concomitant MN inactivation by inhPSAM (Fig. 4, D and E). These results indicate that restoration of synaptic integrity by D(Gs) is not a consequence of increased MN firing, but rather is caused by direct synaptic effects, even if chemogenetic stimulation of MN firing can also induce by itself some synaptic restoration.

Chemogenetic activation of PKA ameliorates disease burden in MNs through firing

Next we assessed whether the activation of the cAMP/PKA pathway, which increased functional and structural integrity of Ia synapses, was associated with a significant effect on MN disease markers. We repeated the D(Gs) experiments with the same experimental groups (Fig. 5 A): acute CNO treatment (one dose, sacrifice after 3 h), chronic CNO treatment (7-d treatment), and control group (saline for 7 d). We considered the burden of misfolded SOD1 (henceforth misfSOD1; using the B8H10 conformation-specific monoclonal antibody), the build-up of LC3A, and the accumulation of p62+ inclusions as disease markers (Rudnick et al., 2017; Martínez-Silva et al., 2018; Ouali Alami et al., 2018). Acute activation of D(Gs) did not reduce levels of misfSOD1 or p62 inclusion burden (in agreement with the slow turnover of these markers; Fig. 5, E and F), but was sufficient to decrease the buildup of LC3A+ autophagic structures (Fig. 5 G). Most importantly, chronic activation of D(Gs) resulted in a robust amelioration of all disease markers (misfSOD, p62 inclusions, and LC3A levels; Fig. 5, E–G). On the other hand, saline-treated D(Gs)+ MNs were comparable to noninfected counterparts in all read-out measures.

Next, we examined whether the effects of the cAMP/PKA pathway on disease markers required the firing of MNs, once again exploiting multiplexed chemogenetics to decrease MN firing (by inhPSAM) while activating PKA (by D(Gs); Fig. 6 A). We evaluated the burden of misfolded SOD1 and LC3A in distinct sets of MNs expressing, as before, either no chemogenetic receptor, D(Gs), inhPSAM, or both. Whereas MNs expressing inhPSAM showed an increased burden of LC3A and misfSOD1 accumulation (although the latter did not quite reach statistical significance in the present work) compared with noninfected MNs (Saxena et al., 2013), MNs expressing D(Gs) displayed a reduced load of both disease markers (Fig. 6, D and E). Most notably, and in contrast to what was observed for synaptic GluR4 and Homer1b, MNs expressing both inhPSAM and D(Gs), in which neuronal firing was reduced while PKA was stimulated, showed no improvements in disease burden compared with noninfected MNs (Fig. 6, D and E).

To demonstrate that the chemogenetic manipulations used above (D(Gs), inhPSAM, actPSAM, and double-chemogenetics inhPSAM + D(Gs)) have a significant impact on the overall activity of the infected MNs, we measured the induction of the immediate-early gene c-fos as a proxy of neuronal activity (Hardingham et al., 1997; Ruediger et al., 2011; Lacar et al., 2016) following an acute injection of the chemogenic agonist (single dose of CNO and PSEM administered 2 h before sacrifice; Fig. 7 A). Compared with uninfected contralateral MNs (Fig. 7 B), reduction of MN firing by inhPSAM did not decrease c-Fos expression (Fig. 7, C and G), probably because of the very low

level in basal conditions. On the other hand, activation of actPSAM (Fig. 7 D) or D(Gs) (Fig. 7 E) resulted in a robust increase in c-Fos levels in the nucleus (Fig. 7 G). Remarkably, concomitant activation of inhPSAM and D(Gs) (Fig. 7 F) significantly decreased c-Fos levels compared with D(Gs) alone (Fig. 7 G), indicating a substantial decrease in neuronal firing. These data verify that the chemogenetic systems are delivering the expected change in MN activity. Thus, whereas the effect of PKA on synaptic structures is independent of MN firing, reducing MN firing largely blocks any beneficial effect of the cAMP/PKA pathway on disease markers.

The excitatory transmission from descending fibers to MNs is also depressed

Having extensively characterized the postsynaptic dysfunction at the Ia synapse, we asked whether this phenomenon was restricted to this particular input or rather generalized. We considered as an alternative source of input, the MLF, which is composed of descending reticulospinal and vestibulospinal fibers, some of which make direct synaptic contacts (VGluT2+; Basaldella et al., 2015) devoid of presynaptic inhibition (Rudomin and Schmidt, 1999) onto lumbar MNs (Liang et al., 2014; Basaldella et al., 2015). In different mice than those used for recording Ia EPSPs, stereotaxic electrical stimulation of MLF in the brainstem evoked a mixture of monosynaptic and disynaptic EPSPs (Fig. 8 A). We focused first on the response to the first shock in a train at 200 Hz, as it was practically uncontaminated by the disynaptic component (see Materials and methods and Fig. S5). Quantification of MLF-evoked EPSPs in MNs revealed a 33% decrease in size in mutSOD1 mice compared with wtSOD1 mice (Fig. 8 B). Second, we quantified the complex response after the fifth shock (that included disynaptic components, unfilled arrowhead in Fig. 8 A). That response was similarly reduced (36% on average; Fig. 8 C), suggesting that most of the decrease could be attributed to the last-order synapses contacting MNs (larger reductions should be expected if other intervening synapses were also affected). As before, the reduction in EPSP size was not due to changes in MN intrinsic properties (Fig. 8, D–F). The similar disruption of Ia synapses and MLF synapses suggests a generalized postsynaptic dysfunction of excitatory synapses on MNs.

Furthermore, we verified that, in correspondence with VGluT2+ terminals (which account for the majority of descending inputs to MNs; Basaldella et al., 2015), the size of the immunolabeled clusters of GluR4, phosphorylated GluR1, and phosphorylated GluR2 were significantly decreased in mutSOD1 MNs (Fig. 8, G–I) compared with WT controls. As with VGluT1+ synapses, we assessed the integrity of the VGluT2+ postsynaptic structure. Because Shank1 and Homer1b were poorly enriched in VGluT2+ synapses (compared with VGluT1+ synapses) we explored the clustering of the Shank2 scaffold protein. Shank2 displayed a punctate pattern, with each cluster juxtaposed to a VGluT2+ terminal, and the size of Shank2 clusters was significantly reduced in mutSOD1 MNs compared with WT counterparts (Fig. 8 J). In line with the model of a substantial postsynaptic site disruption, the size and immunostaining intensity of VGluT2+ terminals demonstrated a small compensatory increase (Fig. 8 K).
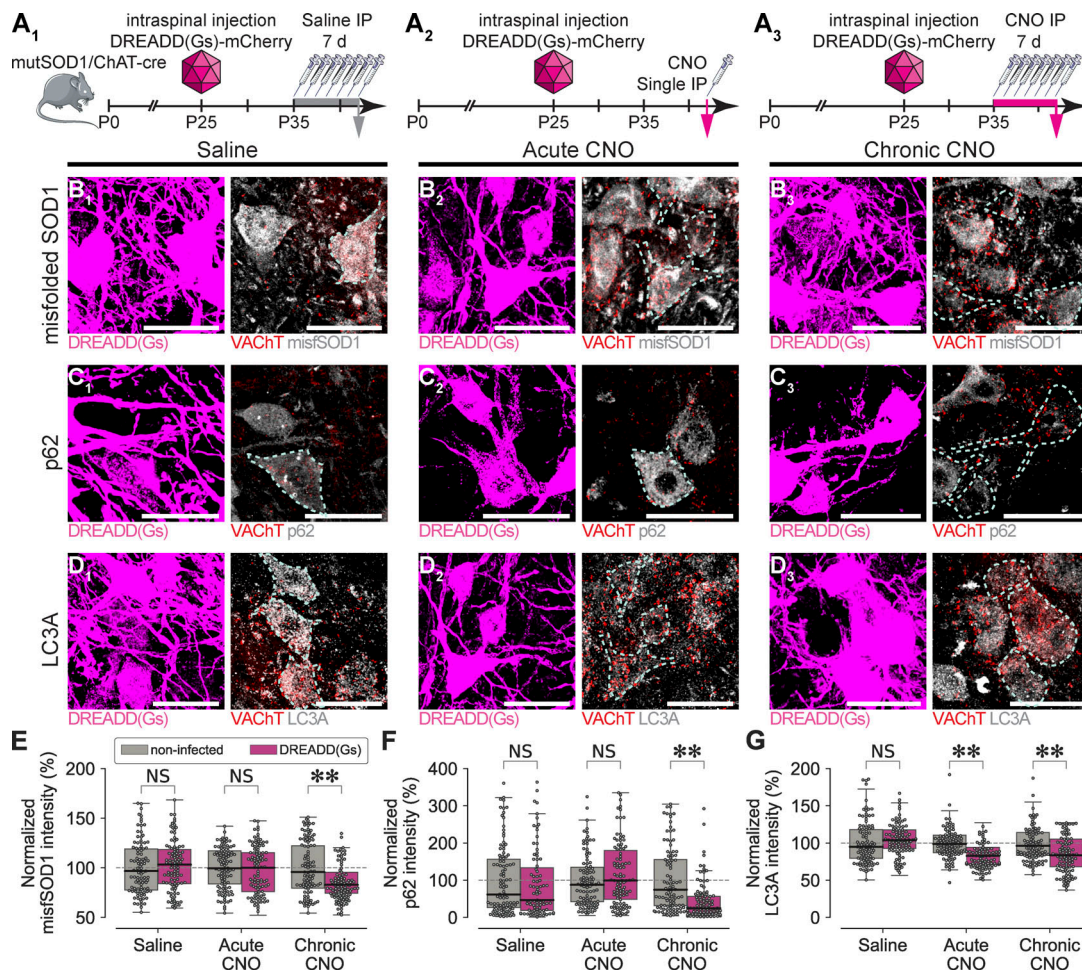
Figure 5. **PKA activation in MNs decreases the disease markers. (A)** Experimental design of vehicle treatment (A_1; three mice), acute activation of the D(Gs) (A_2; three mice), and chronic activation of the D(Gs) (A_3; three mice). **(B)** MNs expressing D(Gs) and immunostained for misfolded SOD1 (B8H10) under vehicle (B_1), acute CNO (B_2), or chronic CNO (B_3) treatment. **(C)** MNs expressing D(Gs) and immunostained for p62 under vehicle (C_1), acute CNO (C_2), or chronic CNO (C_3) treatment. Arrowheads points to p62 aggregates. **(D)** MNs expressing D(Gs) and immunostained for LC3A under vehicle (D_1), acute CNO (D_2), or chronic CNO (D_3) treatment. MNs are identified by VAChT staining. The dotted line represents the approximate outline of the MNs. Scale bars: 20 µm. **(E)** misfSOD1 levels in MNs are decreased in D(Gs)⁺ MNs (magenta) compared with contralateral noninfected MNs (gray) upon chronic CNO treatment (85.3 ± 16.7% of uninfected; two-way ANOVA followed by Tukey HSD, **, P = 0.001), but not upon acute CNO (97.1 ± 23.6% of uninfected) or vehicle treatment (102.0 ± 24.7% of uninfected). Each data point represents a single MN. **(F)** The burden of p62 inclusion in D(Gs)⁺ MNs was not modified by vehicle (90.6 ± 91.7% of contralateral uninfected) or acute CNO (116.2 ± 84.8% of uninfected) treatment but was reduced compared with contralateral noninfected MNs upon chronic CNO treatment (42.9 ± 50.6% of contralateral; Tukey HSD, **, P = 0.001). **(G)** LC3A immunostaining intensity in MNs was unaltered in D(Gs)⁺ neurons compared with contralateral noninfected MNs upon vehicle treatment (104.7 ± 22.2% of uninfected), whereas acute D(Gs) activation (84.8 ± 18.6% of uninfected; Tukey HSD, **, P = 0.001) or chronic D(Gs) activation (84.8 ± 22.9% of uninfected; Tukey HSD, **, P = 0.001) resulted in a significant decrease in LC3A intensity.

Discussion

Our data show that excitatory synaptic inputs to MNs in the mutSOD1 ALS mouse model are functionally reduced and display impaired plasticity already in presymptomatic stages. Structural disruption of the postsynaptic site was identified as a major contributor for these functional disorders. We further show that activation of the cAMP/PKA pathway enhances physiological responses and restores GluR4 content in postsynaptic structures. Importantly, we used a multiplexed-chemogenetic approach to demonstrate that cAMP/PKA effects on synaptic integrity are not a consequence of changes in MN firing, whereas the beneficial effects on disease markers are dependent on neuronal firing. Furthermore, we show that synaptic dysfunction is likely

a generalized phenomenon: decrease in EPSP size characterizes proprioceptive Ia synapses as well as monosynaptic inputs from the vestibulo and reticulospinal tracts (MLF).

Disruption of the postsynaptic side is a major cause of excitatory synaptic failure

The glutamatergic excitotoxicity model predicts a combination of increased intrinsic MN excitability and excessive synaptic or extrasynaptic excitatory stimulation (Rothstein et al., 1990; von Lewinski and Keller, 2005; Bading, 2017) driving abnormal cytoplasmic Ca^{2+} loads and neuronal death. A substantial fraction of clinical trials based on preventing these conditions have failed to deliver beneficial effects (Petrov et al., 2017). Contradicting
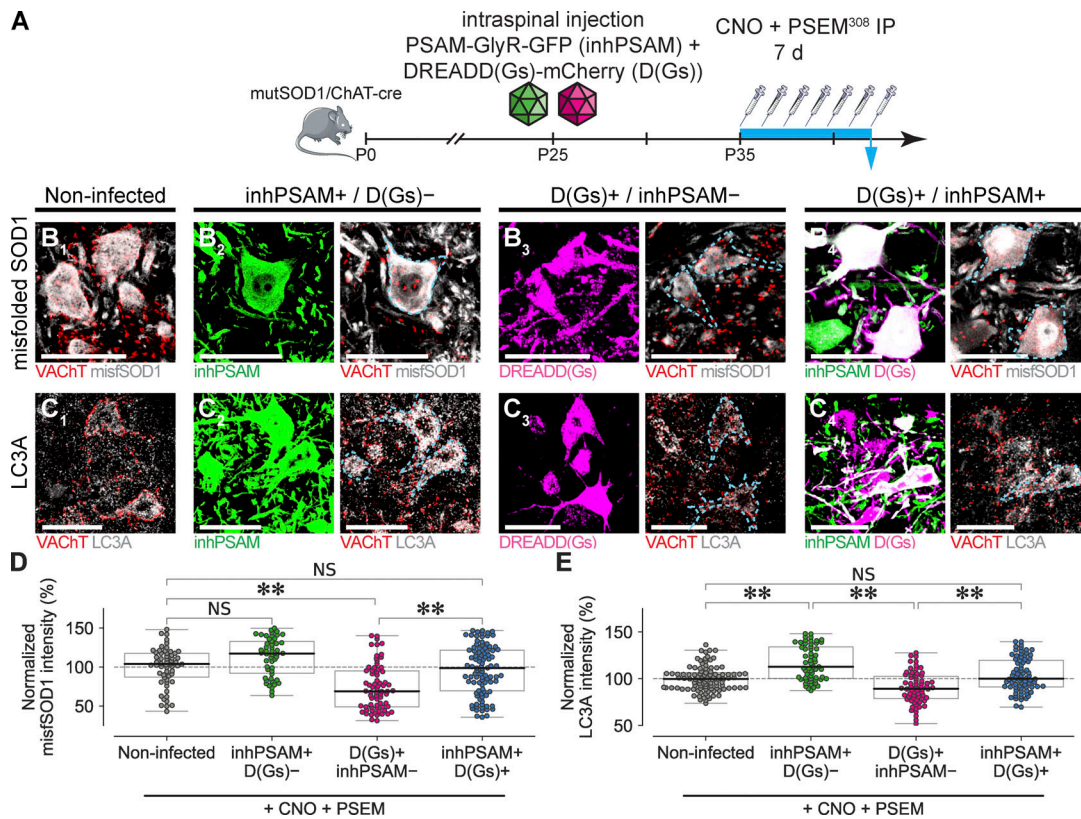
Figure 6. **PKA decreases disease markers through enhanced MN firing. (A)** Experimental design for the double-chemogenetics controls of MN excitation (by inhPSAM) and PKA signaling (by D(Gs)-mCherry) on synaptic levels of misfolded SOD1 proteins and LC3A. **(B)** Representative images of uninfected MN (inhPSAM−/D(Gs)−; B_1), MNs expressing inhPSAM only (inhPSAM+/D(Gs)−, green; B_2), D(Gs) only (D(Gs)+/inhPSAM−, magenta; B_3), or both (D(Gs)+/inhPSAM+, white; B_4) and immunostained for misfolded SOD1 (B8H10). **(C)** Same arrangement of MNs immunostained for LC3A. The outlines of infected MNs are shown with a dashed line. Scale bars: 20 µm. **(D)** Reduction of MN firing by inhPSAM did not significantly affect the misfSOD1 burden (112.9 ± 24.5% of control noninfected; one-way ANOVA followed by Tukey HSD, P = 0.087). In contrast, D(Gs) activation significantly reduced misfSOD1 burden (74.2 ± 29.0% of control uninfected; Tukey HSD, **, P = 0.001). However, reduction of MN firing combined with D(Gs) activation abolished the beneficial effect of the D(Gs) alone (95.9 ± 31.6% of uninfected; Tukey HSD, **, P = 0.001). **(E)** The accumulation of LC3A in MNs was significantly increased upon reduced firing by inhPSAM (116.7 ± 18.3% of control; one-way ANOVA followed by Tukey HSD, **, P = 0.001) and significantly decreased by D(Gs) activation (90.1 ± 16.8% of control noninfected; Tukey HSD, **, P = 0.001); the reduction of MN firing significantly decreased the effect of concomitant D(Gs) activation (103.8 ± 18.0% of control; Tukey HSD, **, P = 0.001). Data from five mutSOD1/ChAT-cre animals per group.

these assumptions, we have previously demonstrated that vulnerable MNs lose their ability to fire repetitively in presymptomatic adult mice (a form of intrinsic hypoexcitability; Delestrée et al., 2014; Martínez-Silva et al., 2018), whereas resistant MNs are intrinsically hyperexcitable at an early stage (Leroy et al., 2014). In these conditions, hyperactive glutamatergic synapses might still drive neurotoxicity by causing large cytoplasmic Ca^{2+} loads even in a condition of normo- or hypoexcitability (Le Masson et al., 2014).

Now we demonstrate that EPSPs are actually decreased in ALS MNs. The reduced clustering of GluR4, phosphorylated GluR1, and GluR2 subunits (in agreement with Ruegsegger et al., 2016) and of postsynaptic scaffold proteins (Shank1 and Homer1b at Ia synapses, Shank2 at VGluT2+ synapses) point to a substantial postsynaptic contribution to the failure of excitatory synapses on ALS MNs. The involvement of a postsynaptic mechanism is further supported by the partial recovery of synaptic structure and function following PKA-pathway activation in the postsynaptic neuron. In contrast, wtSOD1 and mutSOD1 animals exhibited the same level of the classic axo-

axonic presynaptic inhibition of Ia afferents, demonstrating that this pathway cannot account for the changes in EPSP size and paired-pulse ratio in mutSOD1 MNs. Moreover, presynaptic inhibition is restricted to Ia terminals and would not affect MLF terminals (Rudomin and Schmidt, 1999; Fink et al., 2014). Another presynaptic mechanism, the postactivation depression, which is restricted to homonymous Ia afferents (Hultborn et al., 1996), was previously shown to be smaller in mutant SOD1 mice (Hedegaard et al., 2015) and therefore cannot be responsible for the reduced EPSP size. Finally, there are no gross abnormalities in number or constitutive elements of Ia boutons, as shown by immunohistochemical methods. Therefore, the contribution of presynaptic mechanisms, if any, on the synaptic dysfunction might be due to more subtle abnormalities and may be limited in comparison with substantial postsynaptic effects.

We then considered whether Ia synaptic dysfunction may be due to abnormal activity in corticospinal projections (Eisen et al., 2017). Cortical hyperexcitability has been reported in human patients (Vucic and Kiernan, 2006), in cultures (Pieri et al., 2003), and in slices (Saba et al., 2016). In mutSOD1
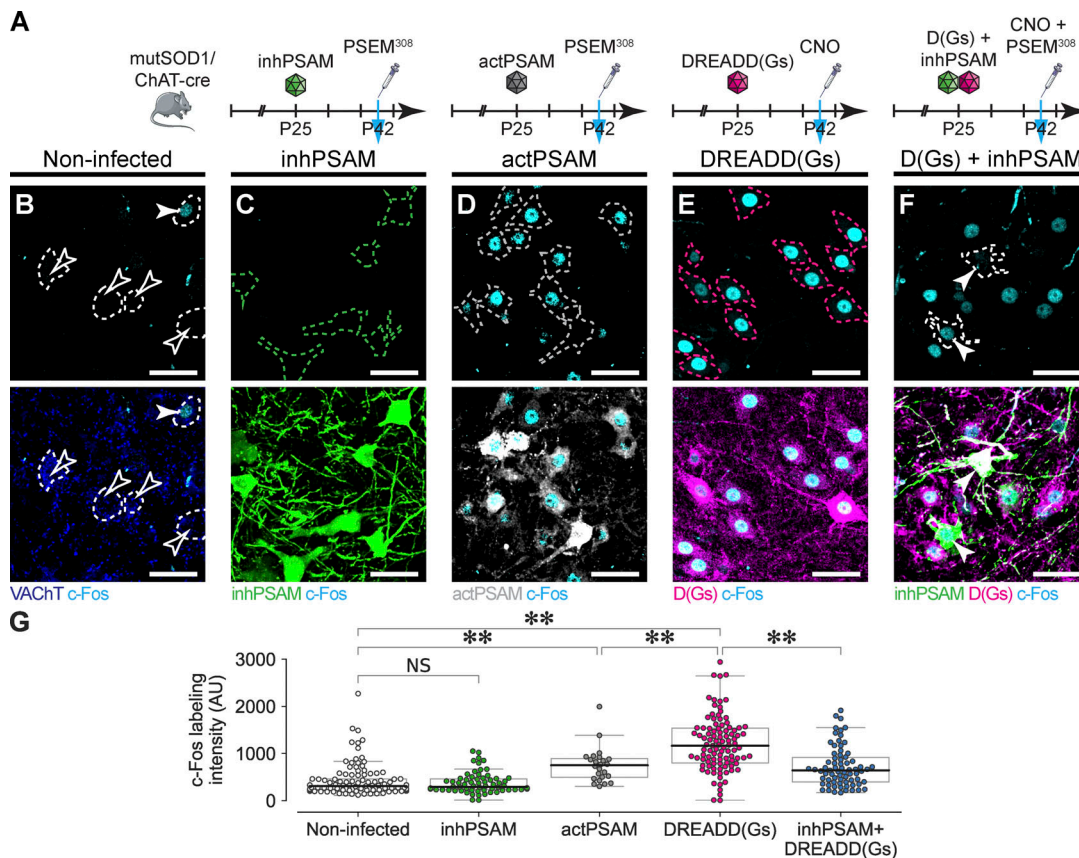
Figure 7. **Chemogenetic manipulations impact the activity of the MNs. (A)** Experimental design for the assessment of single- and double-chemogenetic treatments on c-Fos expression in MNs. **(B)** Little (unfilled arrowhead) or moderate (filled arrowhead) expression of c-Fos in noninfected MNs. **(C)** Because of very low levels at baseline, inhPSAM does not further decrease c-Fos expression. **(D)** Activation of actPSAM significantly increased the expression of c-Fos in infected MNs. **(E)** Activation of DREADD(Gs) significantly increased the expression of c-Fos in infected MNs. **(F)** Double-chemogenetic experiments yielded MNs that were infected solely with AAV encoding D(Gs), a few MNs that were infected solely with inhPSAM (not depicted), and MNs infected by both D(Gs) and inhPSAM AAVs (filled arrowheads). In MNs expressing both inhPSAM and D(Gs), c-Fos levels were significantly lower than in those expressing D(Gs) alone. **(G)** Quantification of c-Fos levels across the different treatments: noninfected: 400 ± 310 AU, $n = 145$; vs. inhPSAM: 369 ± 219 AU, $n = 68$; one-way ANOVA followed by Tukey HSD, $P = 0.9$; actPSAM 750 ± 372 AU, $n = 24$; Tukey HSD, **, $P = 0.001$ vs. noninfected; D(Gs) alone 1,200 ± 569 AU, $n = 103$; Tukey HSD, **, $P = 0.001$ vs. noninfected, and **, $P = 0.001$ vs. actPSAM; D(Gs) + inhPSAM: 720 ± 424 AU, $n = 71$; Tukey HSD, **, $P = 0.001$ vs. D(Gs) alone. In all panels, the dashed lines show the approximate outline of the MN cell bodies. Scale bars: 50 μm. Data are from four independent mutSOD1/ChAT-Cre mice.

mice, the hyperexcitability of corticospinal neurons is restricted to the first postnatal week or to the symptomatic phase (even though, in the latter, hyperexcitability did not result in an altered pattern of calcium events in awake animals), whereas at the age of P40–P50, the excitability of the corticospinal neurons is normal (Kim et al., 2017). Moreover, in mice, the projections from the motor cortex to spinal MNs are not direct and are relayed through the reticulospinal pathway included in the MLF (Alstermark and Ogawa, 2004). Notably, these MLF–MN synapses are actually depressed, as shown in the present work. Thus, cortical hyperexcitability, if any, may not translate into excessive excitation to MNs. Taken together, these findings consistently draw a new model in which vulnerable MNs are not only hypoexcitable but also receive reduced excitation, likely because of postsynaptic dysfunction.

At this presymptomatic stage (around P50), the reduced strength of excitatory synapses is not large enough to impair electromyographic activity or motor performance in all but the most challenging motor tasks (such as walking on an incline;

Akay et al., 2014; Quinlan et al., 2017). Nevertheless, the simultaneous decrease in synaptic strength and intrinsic excitability of MNs could be speculated to interfere with activity-dependent neuroprotective transcriptional programs, leading to vulnerability to disease (Bading, 2013, 2017; Roselli and Caroni, 2015).

cAMP/PKA activation and neuronal firing contribute to synaptic restoration and have a beneficial impact on the ALS-related pathobiochemistry

We show that before muscle denervation, the disruption of Ia synapses (both EPSP size and GluR4 and Homer1b content) is reversible by postsynaptic PKA activation. This is in agreement with the critical role of PKA in phosphorylating Ser842 (corresponding to Ser862 in the mouse) on the GluR4 C-terminus, enhancing its synaptic insertion (Esteban et al., 2003; Gomes et al., 2007; Diering et al., 2014). In addition, the restoration of Homer1b clusters appears to be a direct effect of cAMP/PKA, in agreement with the enhanced Homer1b clustering induced by
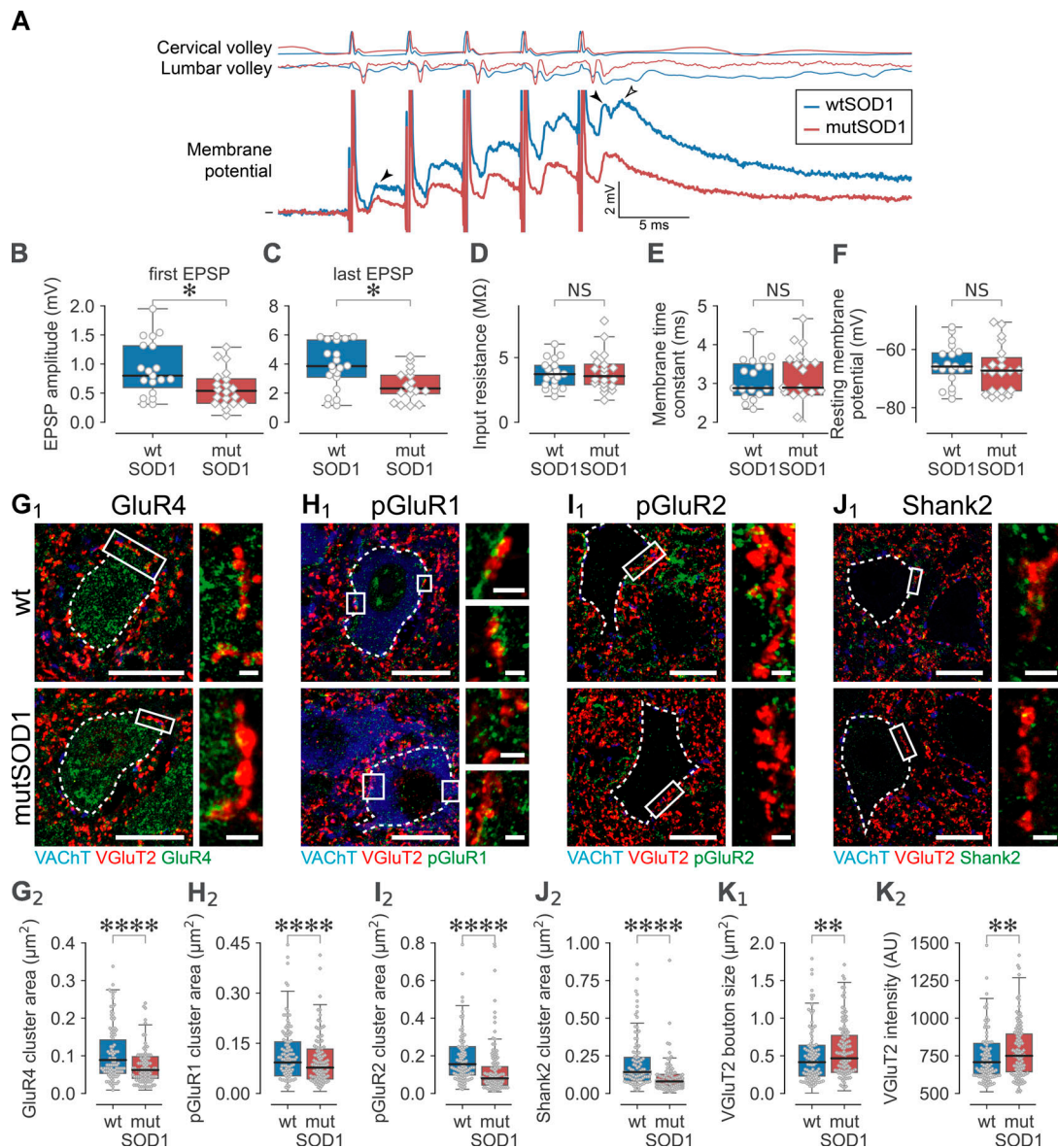
Figure 8. **Impairment of descending EPSPs evoked by MLF stimulation and of VGlut2 postsynaptic structures on MNs. (A)** Superimposed recordings from a wtSOD1 and a mutSOD1 MN in response to a 200-Hz train stimulation of the MLF repeated at 3 Hz. The responses displayed a mixture of monosynaptic (black arrows) and disynaptic (unfilled arrow) EPSPs. Note that the first shock in the train elicited essentially a monosynaptic response. Top trace: Volley recorded at the cervical level. Middle trace: Volley recorded at the lumbar level. Bottom trace: Membrane potential of the MN. Stimulation artifacts were truncated. **(B)** Comparison of the amplitude of the first (monosynaptic) EPSP of the train. wtSOD1: 0.9 ± 0.5 mV, n = 19; vs. mutSOD1: 0.6 ± 0.3 mV, n = 20; MW, *, P = 0.022. **(C)** Comparison of the amplitude of the last EPSP of the train (late response of the complex EPSP that includes nonmonosynaptic components, unfilled arrowhead). wtSOD1: 3.9 ± 1.6 mV; n = 21; vs. mutSOD1: 2.5 ± 1.1 mV; n = 17; MW, *, P = 0.012. **(D)** The input resistance was not significantly different between wtSOD1 and mutSOD1 MNs: 3.9 ± 1.5 MΩ, n = 20; vs. 3.7 ± 1.1 MΩ, n = 19; t test, P = 0.71. **(E)** The membrane time constant was not significantly different between wtSOD1 and mutSOD1 MNs: 3.1 ± 1.0 ms, n = 20; vs. 3.0 ± 0.7 ms, n = 19; t test, P = 0.84. **(F)** The resting membrane potential was not significantly different between wtSOD1 and mutSOD1 MNs: −66.7 ± 8.2 mV, n = 20; vs. mutSOD1: −65.2 ± 7.0 mV, n = 19; t test, P = 0.54. Each point on the graphs represents one MN. Experiments were performed in seven mutSOD1 mice and six wtSOD1 mice. **(G–J)** The postsynaptic side of VGluT2+ synapses was disrupted. Each panel shows a large view of the MN (scale bar: 20 μm) with a zoom of the region(s) inside the box(es) in inset (scale bars: 2 μm). The dashed lines show the approximate contour of the MN cell bodies. **(G)** GluR4 cluster area was significantly reduced in mutSOD1 MNs: 0.08 ± 0.05 μm², n = 980; vs. WT: 0.11 ± 0.07 μm², n = 780; t test, ****, P = 1.8 × 10⁻²⁵. **(H)** Phosphorylated GluR1 cluster area was also significantly decreased: mutSOD1: 0.10 ± 0.08 μm², n = 986; vs. WT: 0.12 ± 0.09 μm², n = 989; t test, ****, P = 1.1 × 10⁻⁵. **(I)** Phosphorylated GluR2 cluster area was reduced compared with controls: mutSOD1: 0.11 ± 0.11 μm², n = 487; vs. WT: 0.19 ± 0.13 μm², n = 478; t test, ****, P = 3.0 × 10⁻²². **(J)** The cluster area of the postsynaptic scaffolding protein Shank2 was reduced in mutSOD1 MNs compared with controls: mutSOD1: 0.10 ± 0.08 μm², n = 587; vs. WT: 0.20 ± 0.19 μm², n = 604; t test, ****, P = 6.5 × 10⁻²⁷. **(K)** In contrast, the size and labeling intensity of the presynaptic VGluT2+ boutons was slightly increased in mutant animals. mutSOD1 VGluT2 bouton size: 0.57 ± 0.38 μm², n = 587; vs. WT: 0.50 ± 0.37 μm², n = 586; t test, **, P = 0.004 (K_1); mutSOD1 VGluT2 labeling intensity: 791 ± 194 AU, n = 587; vs. WT: 757 ± 185 AU, n = 586; t test, **, P = 0.0017 (K_2).

phosphodiesterase inhibition (an alternative approach to increase cAMP levels; Shiraishi et al., 2003) and may hint at broader consequences on synaptic structures regulated by PKA (Lu et al., 2011).

Furthermore, we show that the beneficial effects of cAMP/PKA activation extend to multiple markers of mSOD1/ALS pathobiochemistry. We have exploited a multiplexed chemogenetic strategy, based on the simultaneous expression and activation of the mutually orthogonal PSAM/PSEM system (Magnus et al., 2011) and the DREADD system (Roth, 2016), to show that decreasing MN excitability largely prevents the recovering actions of cAMP/PKA on disease markers but not on synaptic composition. It should be noted, however, that reducing MN firing by inhPSAM resulted in a small increase in synaptic GluR4 (but not Homer1b) levels. We hypothesize that such an effect may bear similarity to the up-regulation of AMPAR occurring as homeostatic scaling upon chronic blockade of neuronal firing (O'Brien et al., 1998; Turrigiano et al., 1998; Diering et al., 2014). Notably, Homer1b levels are unaffected, suggesting that the hypothesized homeostatic response may be weak. Although it has been previously shown that cAMP/PKA promotes proteasomal degradation of misfolded SOD1 by phosphorylating the Rpn6 subunit of the 26S proteasome (Lokireddy et al., 2015; VerPlank et al., 2019), the activity-dependent nature of the effect of PKA on misfolded SOD1, LC3A, and p62 suggests that it may be mediated by excitation-controlled transcription factors controlling the expression of autophagy and proteasome proteins, e.g., cAMP response element binding protein (Seok et al., 2014; Wang et al., 2015). Increasing MN firing by chemogenetically controlled cation channels (Magnus et al., 2011) also results in a degree of restoration of GluR4 and Homer1b content in synapses and was previously reported to evoke similar beneficial effects on disease markers (Saxena et al., 2013). Taken together, these findings support a model in which cAMP/PKA activation restores synaptic integrity, which in turn improves MN recruitment and firing, reducing the burden of disease markers (Fig. 9).

These findings suggest the existence of a "vicious circle" at work: the pathogenic *primum movens* may cause an initial disruption of synapses and, in parallel, reduced MN excitability (Delestrée et al., 2014; Martínez-Silva et al., 2018). We hypothesize that disturbed intracellular trafficking by misfSOD1 (Hadano et al., 2010; van Dis et al., 2014; Soo et al., 2015) may be at the origin of the large dendritic vacuoles, and these abnormal structures may weaken synapses by sequestering glutamate receptors. These two events would reduce MN firing, which would in turn further worsen cellular abnormalities (including trafficking impairment, autophagy overload, and endoplasmic reticulum stress) and further accelerate the disruption of synapses and firing, precipitating the demise of the MN itself. The demonstration that PKA activation restores synaptic integrity and then leads to the activity-dependent beneficial effects on disease markers shows that this vicious circle can be interrupted by acting at a single-pathway level. However, the focal nature of intraspinal injections and the comparatively small number of MNs affected has limited the assessment of long-term effects of PKA activation on mouse survival. Nevertheless, we show the
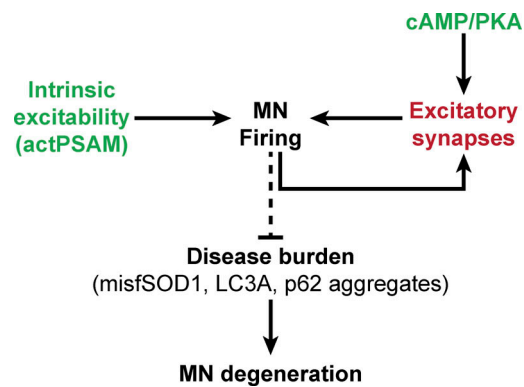

Figure 9. **Schematic representation of the main findings.** Chemogenetic interventions (in green) on intrinsic excitability (using actPSAM) and dysfunctional excitatory synapses (in red) through the cAMP/PKA pathway converge to restore adequate MN firing, which in turn reduces the burden of cellular abnormalities that drives MN degeneration.

impact of PKA activation on different disease markers whose decrease has been repeatedly correlated with prolonged survival (e.g., Saxena et al., 2013; Ouali Alami et al., 2018).

Together with the previously reported hypoexcitability of MNs, the early impairment of excitatory synaptic function depicts a new conceptual framework for excitation-dependent processes in ALS, in which loss of activity-dependent neuroprotection, rather than excitotoxicity, shapes MN vulnerability. Interventions at the motoneuronal synaptic level, potentially aimed at the cAMP/PKA pathway, emerge as viable new strategies for early ALS management.

Materials and methods
Animals
Animals for electrophysiological experiments were bred and housed in the BioMedTech animal facility at Université de Paris. Electrophysiological procedures were approved by the Paris Descartes University ethics committee (CEEA34; authorization number CEEA34.MM.064.12) and followed the European Directives (86/609/CEE and 2010-63-UE) and the French legislation on the protection of animals used for scientific purposes. Two lines of transgenic mice were used: B6SJL-Tg(SOD1*G93A)1Gur/J (called mutSOD1 here), which carry a mutated human *SOD1* gene and have a phenotype similar to late-onset ALS in humans, and B6SJL-Tg(SOD1)2Gur/J (called wtSOD1 here), which carry the nonmutated human *SOD1* gene and display no pathological phenotype. In both lines, the transgene copy number was measured by quantitative PCR and found to be >20. Both male and female mice were used for electrophysiological recordings. MNs recorded from mutSOD1 mice were compared with the ones recorded from wtSOD1 mice. Experiments were performed on mice at age P45–P55 (presymptomatic young adult animals), unless otherwise specified.

The chemogenetic experiments and the quantitative immunohistological analyses were performed at Ulm University in compliance with institutional guidelines (Tierforschungszentrum, Ulm) and German animal protection laws, approved by

Bączyk et al.
Synaptic neuroprotection in ALS

Journal of Experimental Medicine 13 of 20
https://doi.org/10.1084/jem.20191734

Regierungspräsidium Tübingen (Tübingen, Germany), under license no. 1404. The breeding and the sacrifice of mutSOD1 mice in Ulm was approved by the local veterinary service and animal experimentation oversight committee under license no. 1312. For the chemogenetic experiments, high-copy B6SJL-Tg(SOD1*G93A)1Gur/J mice (obtained from Jackson Laboratory) were crossed with homozygous ChAT-cre females (kind gift from Pico Caroni, Friedrich Miescher Institute for Biomedical Research, Basel, Switzerland) and the F1 offspring mutSOD1/ChAT-cre double-tg mice were used for experiments. Only male mice were used in chemogenetics and histological experiments to minimize the between-subject variability (Ouali Alami et al., 2018). *Gria4* knockout mice (B6.129P2-*Gria4*^tm1Dgen; *Gria4*^−/− for brevity) were backcrossed to the C57BL/6J strain for 10 generations and then maintained as a homozygous colony; these mice have been previously characterized (Beyer et al., 2008). WT C57BL/6J (*Gria4*^+/+) mice were used as controls in the experiment involving *Gria4*^−/− mice.

Surgery for electrophysiological experiments

The surgical procedures have been described previously (Manuel et al., 2009; Delestrée et al., 2014). Briefly, atropine (0.20 mg/kg; Aguettant) and methylprednisolone (0.05 mg; Solu-Medrol; Pfizer) were given subcutaneously at the onset of the experiment, to prevent salivation and edema, respectively. 15 min later, anesthesia was induced with an i.p. injection of sodium pentobarbitone (70 mg/kg; Pentobarbital; Sanofi-Aventis). A tracheotomy was performed, and the mouse was artificially ventilated with pure oxygen (SAR-830/AP ventilator; CWE). The end-tidal CO_2 level was maintained at ~4% (MicroCapstar; CWE). The heart rate was monitored (CT-1000; CWE), and the central temperature was kept at 37°C using an infrared heating lamp and an electric blanket. A catheter was introduced in the external jugular vein, allowing us to supplement the anesthesia whenever necessary (usually every 20–30 min) by i.v. injection (sodium pentobarbitone, 6 mg/kg). The adequacy of anesthesia was assessed by lack of noxious reflexes and stability of the heart rate (usually 400–500 bpm) and end-tidal PCO_2. A slow i.v. infusion (50 μl/h) of a 4% glucose solution containing $NaHCO_3$ (1%) and gelatin (14%; Plasmagel; Roger Bellon) helped maintain the physiological parameters. The animal was paralyzed after the surgery with pancuronium bromide (Pavulon; Organon; initial bolus was 0.1 mg, followed by a continuous infusion 0.01 mg/h). Additional doses of anesthetic were then provided at the same frequency as before the paralysis, and adequacy of anesthesia was assessed by stability of the heart rate and PCO_2. The vertebral column was immobilized with two pairs of horizontal bars (Cunningham Spinal Adaptor; Stoelting) applied on the Th12 and L2 vertebral bodies, and the L3–L4 spinal segments were exposed by a laminectomy at the Th13–L1 level. The tissues in the hindlimb and spinal cord were covered with pools of mineral oil.

Stimulation and recording

The MNs were impaled with micropipettes (tip diameter, 1.0–1.5 μm) filled with a mixture of 2 M K-acetate and 0.1 M QX-314 (sodium channel blocker; Sigma-Aldrich). Recordings were made using an Axoclamp 2B amplifier (Molecular Devices)

connected to a Power1401 interface (sampling rate 20 kHz) and using Spike2 software (CED). After impalement, identification of MNs rested on the observation of antidromic action potentials in response to the electrical stimulation of their axon in the triceps nerve. This method of identification was still possible despite the QX-314, as it takes ~30–90 s for the compound to diffuse from the tip of the electrode to the cell body to block the sodium channels. All MNs retained for analysis had a resting membrane potential more hyperpolarized than −50 mV and an overshooting action potential >65 mV. As fully described in Manuel et al. (2009), the input resistance was measured using the peak response of a series of small-amplitude square current pulses (−3 to +3 nA, 500 ms), and the membrane time constant was measured on the relaxation of the membrane potential after injection of small hyperpolarizing current pulses (−5 nA, 1 ms). All recordings were performed in bridge mode, except for the input resistance, which was recorded using discontinuous current clamp mode (7–9 kHz). All care was taken to compensate for the microelectrode resistance and capacitance. At the end of the experiments, animals were killed with a lethal i.v. injection of pentobarbitone (200 mg/kg).

Vibration experiments

After initial surgery, the triceps nerve (composed of the nerves innervating medial gastrocnemius, lateral gastrocnemius [LG], and soleus muscles) was separated from the surrounding tissues and mounted on a silver bipolar electrode for stimulation and electroneurogram (ENG) recording. The triceps muscle belly was separated from the surrounding tissues, and the Achilles tendon was cut free at the triceps insertion point as close to the heel as possible. The tendon was connected with a rigid suture to the center of a loudspeaker membrane driven by a function generator. Before the tendon was cut, the mouse paw was dorsiflexed to the maximum flexion angle, and a small mark was made on the bone to indicate the muscle's maximum physiological length. After the transfer of the tendon to the vibrator, the muscle was stretched to mimic the maximum length during dorsiflexion. The Achilles tendon was vibrated at frequencies ranging from 300 to 500 Hz. For each MN, we searched for the vibration frequency that elicited the largest EPSP (370 Hz, on average). The obtained signal was smoothed using root mean square amplitude (Spike2, time constant 4 ms), and then peak amplitude of the response was measured.

Electrically evoked EPSPs and paired-pulse protocol experiments

In these experiments, the surgery was similar to the previously described vibration experiments, with the exception of Achilles tendon dissection. After MN penetration and identification, the triceps nerve was stimulated with constant-current pulses of 20-μs duration repeated at 3 Hz. The intensity of stimulation was gradually increased from the threshold (minimal intensity to recruit the most excitable afferents as seen by the apparition of a volley response recorded at the surface of the spinal cord) up to the point when maximum amplitude of EPSP was reached (Fig. S1, A and B). 10–30 successive sweeps at the stimulation intensity that elicited the maximal EPSP (usually 1.8× to 2.0×

threshold) were averaged offline, and measurements were obtained from these averages. In the paired-pulse experiments, the nerve was stimulated with a pair of constant current pulses separated by 10-ms intervals at an intensity that elicited submaximal EPSPs amplitudes. The sequence was repeated at 3 Hz ≥10 times. For each MN, we computed the paired-pulse ratio for each individual pair and then averaged the individual ratios. To investigate the presynaptic inhibition of Ia terminals, the Ia EPSP in TS MNs elicited by stimulation of the TS nerve (test response) was conditioned by stimulating group I afferents in the nerve branches innervating the posterior part of the biceps femoris (three shocks at 200 Hz; 2× threshold of the most excitable afferents; conditioning stimulation applied 23 ms before the test stimulation). Renshaw inhibition was observed in separate experiments in which the L4–L5 dorsal roots were cut to suppress the sensory EPSPs. In these conditions, stimulation of the TS nerve produces only an inhibitory postsynaptic potential elicited by the motor axon collaterals.

Stimulation of the descending tracts

These experiments were performed on a separate set of animals from those in the Ia EPSP experiments above. After initial surgery (laminectomy and nerve dissection as described above), a craniotomy was performed over the cerebellum, ~1 mm caudal with respect to the lambda landmark, and an additional laminectomy over C7–Th1 spinal segments was performed for descending volley recording. A tungsten stimulating electrode (WPI, tip 1 µm, resistance 1 MΩ) was inserted into the mouse brainstem through the cerebellum, at the stereotaxic coordinates anteroposterior –7.2, mediolateral +0.1 with reference to the bregma landmark, using a Neurostar robot stereotaxic instrument. At this location, the MLF contains reticulospinal, tectospinal, and vestibulospinal fibers. The vestibulospinal and reticulospinal fibers make direct monosynaptic connections with TS MNs in mice (Liang et al., 2014). The MLF was stimulated with single constant-current shocks of 150-µs duration delivered through the descending tungsten electrode against the reference electrode located in the temporal muscles. The smallest stimulation intensity (threshold intensity) to elicit a volley in the cervical cord and in the lumbar cord was never stronger than 25 µA (average 14.3 µA, SD 5.7 µA). Correct placement of the electrode was assessed while monitoring the descending volley at the C7 and L3 spinal levels. The electrode was placed at the depth at which the descending volley was maximal (Fig. S5, A and B).

Upon successful penetration of an MN, the MLF was stimulated with a train of five pulses at 200 Hz, repeated at 3 Hz. We then recorded EPSPs in spinal MNs at 2.2× threshold intensity (the final intensity was always <60 µA; intensity at which the current spread from the tip of the electrode was <0.25 mm [Gustafsson and Jankowska, 1976] only activating MLF). We recorded 10–30 sweeps, which were averaged, and measurements were made on these averages. In a few cells (four wtSOD1 and six mutSOD1), the MLF stimulation evoked only a monosynaptic response, as exemplified in Fig. S5 D. The latency between the descending volley recorded at the lumbar level and the EPSP onset was short (0.3 ms in the example of Fig. S5 D). In

such a short delay, there is no time for the activation of an interposed interneuron, indicating that the descending fibers synapse directly onto the MN. In extremely rare instances (one wtSOD1 and one mutSOD1 cell not included in the analysis of monosynaptic inputs), we observed solely a disynaptic EPSPs (Fig. S5 E). Disynaptic EPSPs appeared only after the second shock (unfilled arrow, no EPSP visible in response to the first shock), and they grew in response to the following stimulations, indicating a progressive temporal facilitation of an increasing number of interposed excitatory interneurons. The central latency with respect to the fastest component in the volley was 1.4 ms, i.e., ~1 ms longer than the monosynaptic response (this supplemental delay is caused by the activation of the synapses to interneurons, the time for interneurons to reach their firing threshold, and the axonal conduction velocity of interneurons, which might be slower than the axonal conduction velocity of descending fibers). However, in most MNs (15 wtSOD1 and 14 mutSOD1), the responses were mixed (Fig. 8 A): after the peak of the monosynaptic component (filled arrowheads), a bump was visible, reflecting the apparition of the disynaptic component (unfilled arrowhead). However, this disynaptic component was negligible in the response to the first stimulation of the train.

At the end of the experiment, the location of the electrode was marked by an electrolytic lesion, the mouse was perfused intracardially with 4% paraformaldehyde (PFA), and the brainstem was removed, cut at 100 µm on a vibrating microtome (model 7000smz-2, Campden Instruments), and stained with Cresyl violet. The lesion location was verified with light microscopy (Fig. S5 C).

PKA activation experiments

Initial surgery and MN stimulation and recording were performed as described above. To measure the impact of PKA activation on MN synaptic excitation levels, the recording microelectrode was filled with a mixture of 2 M K-acetate, 0.1 M QX-314, and 4 mM cAMP analogue (S)-adenosine, cyclic 3′,5′-(hydrogenphosphorothioate) triethylammonium (cAMPS-Sp). Next, EPSP amplitude and paired-pulse ratio were measured before, immediately after, and in successive 2-min intervals after iontophoretic injection of cAMPS-Sp through the microelectrode (500-ms pulses of –2 to –4 nA, repeated at 1 Hz, total amount injected –120 to –180 nA • s; Lalley et al., 1997).

Intracellular labeling of MNs and immunostaining of Ia synaptic contacts

The surgery and intracellular recordings of TS MNs were performed as above. The microelectrode was filled with a mixture of 3 M KCl and 2% Neurobiotin (Vector Laboratories). A series of current pulses (2–5 nA, 600 ms, 1 Hz), was used to transfer the neurobiotin into the MN. 45 min after injection, to allow the neurobiotin to diffuse in distal dendrites, the mouse was perfused intracardially, using 50 ml of 1× PBS and 100 ml of 4% PFA. The spinal cord was postfixed for 1 h and then preserved in 1× PBS. The spinal cord was embedded in 4% agarose and cut in 50-µm slices with a vibratome (VT1000S, Leica). Slices were incubated for 1 h in 1× PBS, 3% Triton X-100, BSA (5 mg/ml), and 10% donkey serum and then rinsed three times for 10 min with

PBS. The Neurobiotin was revealed by incubation of the slices in 1× PBS, 1% Triton X-100, BSA (5 mg/ml), and Streptavidin-Cy3 (1:500, Sigma-Aldrich). After rinsing three times for 10 min, slices were incubated overnight at 4°C in 1× PBS, 1% Triton X-100, and BSA (5 mg/ml) with primary antibodies anti-VGluT1 (guinea pig, 1:4,000, Merck Millipore). Slices were rinsed three times for 10 min again, and secondary antibodies Alexa Fluor 647–conjugated donkey anti-guinea pig (1:500, Jackson Immunoresearch Laboratories) were applied in 1× PBS, 1% Triton X-100, and BSA (5 mg/ml) for 3 h at room temperature. Finally, slices were washed three times for 10 min with PBS and mounted on slides with Fluoroshield. Slides were then analyzed using a confocal microscope for fluorescence (LSM710; Carl Zeiss). For the somatic synaptic density, cholera toxin subunit B coupled to Alexa Fluor 488 (10 µl, 2% CTb-488 in sterile water) was injected into the right LG muscles at P50 (n = 3 WT and 3 mutSOD1 mice). 4–5 d later, the animals were perfused with 4% PFA, and immunolabeling against VGluT1 was performed as above. Z-stacks of somas were acquired on a LSM710 confocal microscope with a 63× oil-immersion objective. The images were processed in Neurolucida, and a 3D model of the soma surface was constructed while counting the number of boutons in juxtaposition to the soma.

Chemogenetic experiments

The AAV9 encoding pAAV(9)-pCAG-A7-floxed-PSAM(L141F, Y115F)5HT3-WPRE, and pAAV(9)-pCAG-A7-floxed-PSAM(L141F, Y115F)-GlyR-GFP-WPRE (Magnus et al., 2011) were prepared by Vector Biolabs. The plasmid encoding pAAV-hSyn-DIO-rM3D(Gs)-mCherry was obtained from Addgene (plasmid #50458), and the plasmids encoding the capsid protein for WT AAV9 and the *rep* gene were a kind gift of Oliver Müller (University of Kiel, Kiel, Germany); the AAV9 preparation was performed as previously reported (Commisso et al., 2018). All AAV vectors were prepared in stock suspensions at the titer of 1×10^{13} genomes/ml.

The intraspinal injection of single AAV9 vectors for the expression of the chemogenetic PSAM or DREADD receptors and the chemogenetic agonist treatment were performed as previously reported (Saxena et al., 2013). This approach was chosen because it yields a large number of infected MNs at the injection site (Fig. S4 A). However, the volume injected was purposefully kept small to (i) minimize the surgical and injection injury to the juvenile spinal cord and (ii) minimize the discomfort to the experimental animal that may result from excessive or reduced excitability of a number of MNs. Consequently, only a spinal cord segment 200–300 µm long contained infected MNs. Briefly, animals were placed in a stereotaxic frame under buprenorphine (0.1 mg/kg)/meloxicam (1.0 mg/kg) premedication and continuous 4% sevoflurane anesthesia (in 96% O_2 at 0.8 liter/min). After incision of the skin and the subcutaneous fascia, the paraspinal muscles were blunt dissected, and the dorsal laminae of the T11–T12 vertebrae were incised with a corneal-limb scissor (Fine Science Instruments). The bone flap was removed to expose the dorsal aspect of the spinal cord. Using the dorsal artery as reference, a pulled glass capillary was lowered using the stereotaxic frame at the coordinates y = +0.25 mm z = −0.4 mm at one location in the lumbar spinal cord.

Approximately 0.5 µl total AAV suspension (titer 1×10^{13} genomes/ml) was mixed with 0.5 µl of 1.5% Fast-green and injected (at 0.1 µl/min) using a PicoSprizer III (Parker) microfluidic device. For the double-chemogenetic experiments, 0.5 µl of AAV9-PSAM suspension and 0.5 µl of AAV2-9-DREADD Gs suspension were mixed together with 1 µl of 1.5% Fast-green; a volume of 1 µl from the mix was then injected. The capillary was left in place for 10 min after the end of the injection. After retraction of the capillary, the paraspinal muscles were sutured on the midline using Prolene 6/0 surgical thread, the fascia was positioned on the midline, and overlying skin was sutured with Prolene 6/0. Mice were administered buprenorphine (0.05 mg/kg) twice per day and meloxicam (1.0 mg/kg) daily for three consecutive days after surgery. The chemogenetic agonist PSEM[308] (Apex Scientific) was administered s.c. at a dose of 5 mg/kg in saline. CNO (Tocris) was administered at a dose of 5 mg/kg diluted in saline. For chronic experiments, the agonist was injected once per day starting 10 d after AAV injection for 7 d. For acute experiments, a single dose was administered on the day 17 after AAV injection. Mice were sacrificed 3 h after the last administration of the agonist.

Immunostaining of pre- and postsynaptic structures

All histological evaluations were performed on mutSOD1 or nontransgenic littermates (called WT here). Mice were terminally anesthetized with cloralium hydrate and transcardially perfused with 50 ml ice-cold PBS followed by 2.5–3 ml/g of 4% PFA in PBS (pH 7.4). Spinal cord samples were quickly dissected and postfixed in 4% PFA in PBS at 4°C for 18 h, washed in PBS, and cryoprotected in 30% sucrose in PBS for 36 h. Samples were then snap-frozen in optimal cutting temperature compound and sectioned at −18°C in a cryostat (Leica CM1950); 40-µm-thick sections were washed in PBS and used for immunostaining. Free-floating spinal cord sections were incubated in blocking buffer (3% BSA and 0.3% Triton), followed by incubation with opportune primary antibody (diluted in blocking buffer): anti-VAChT 1:300, Millipore ABN100 (for goat anti-VAChT immunostaining, we diluted the primary antibody directly in a BSA-free solution made with PBS and 0.3% Triton X-100 [Thermo Fisher Scientific], avoiding the blocking step); anti-VAChT 1:300, SYSY 139105; anti-misfolded SOD1 B8H10 1:500, Biomol MM-0070-P; anti-LC3A 1:300, Cell Signaling D50G8 4599, anti-RFP Atto 565 1:500, Nanotag Biotechnologies At565-S; anti-GFP 1:500, Abcam ab13970; α-bungarotoxin CF 405S conjugate 1:500, Biotium 00002; anti-pGluR1 1:100, Abcam ab12108; anti-pGluR2 1:200, Abcam ab52180; anti-VGluT1 1:500, SYSY 135304; anti-bassoon 1:500, Enzo VAM-PS003; anti-synaptophysin 1:200, SYSY 101002; anti-Homer1b/c 1:500, SYSY 160023; anti-Shank1 1:200 Novus NB300-167.500; anti-Shank2 1:500 (previously reported [Peter et al., 2016]; kind gift from Tobias Boeckers, Institute of Anatomy and Cell Biology, Ulm University); anti-GluR4 1:500, Cell Signaling Technologies D41A11 8070; anti c-Fos [2H2] 1:500, Abcam ab208942; for 48 h at 4°C. The specificity of the antibody against GluR4 was tested on cerebellar sections of WT and *Gria4*^{−/−} mice. The molecular layer was brightly stained by the anti-GluR4 antibody in WT animals, but the staining was reduced to background levels in *Gria4*^{−/−} mice (Fig. S4, G and H). Spinal cord sections were thereafter washed three times for 45 min in PBS and 0.1% Triton

X-100, incubated for 2 h at room temperature with the opportune secondary antibody combination (all diluted at 1:500: donkey anti-goat Alexa Fluor 405, Abcam ab175664; donkey anti-guinea pig CF-633, Biotium 20171; donkey anti-rabbit Alexa Fluor 488, Life Technologies A-21206; donkey anti-rabbit Alexa Fluor 647, Life Technologies A-31573; donkey anti-mouse Alexa Fluor 488, Alexa Fluor 568, and Alexa Fluor 647, Life Technologies A-21202, A-10037, and A-31571; donkey anti-chicken Alexa Fluor 488, Jackson Immunoresearch 703–545-155) and mounted in ProLong Gold Antifade (Thermo Fisher Scientific).

Fluorescent images were acquired with a Zeiss 710 confocal microscope, with a 63× oil-immersion objective (NA 1.40) and 2.5 added optical zoom; optical section thickness was set at 200 nm; and images were acquired at 12-bit depth. Acquisition parameters were adjusted so as to maintain fluorescence intensity from target structures below saturation and above zero values; imaging parameters were kept constant across replicates and genotypes. α-MNs were identified by their VAChT-positive cytoplasm surrounded by bright VAChT-positive C-boutons and displaying a VAChT-negative area at the center of the cell corresponding to the nucleus. This strategy allows the exclusion of γ-MNs, which are devoid of C-boutons. The combined use of cytoplasmic VAChT immunostaining and C-boutons lining, together with the identification of the nuclear halo, allows the definition of the cellular contour and the establishment of the spatial orientation of synaptic structures. The postsynaptic structures located between the presynaptic terminal and the cytoplasm of the cell are considered to belong to the identified MN, whereas those located in proximity of the presynaptic terminal but away from the cytoplasm are considered to belong to other structures or cells and were excluded from the analysis. For a better display, the contrast of the representative pictures was adjusted to highlight mainly the bright C-boutons rather than the relatively dimmer cytoplasmic VAChT staining (see Fig. S2, E and F, for examples in which the VAChT signal was intentionally boosted to highlight the cytoplasmic labeling). MNs for analysis were selected randomly in the lateral pool of the ventral horn from spinal cord sections (at L3–L5). Confocal stacks were acquired starting at a depth of 4 μm below the surface of the section; 10–15 optical sections were acquired for each MN. Spinal cord sections displaying cutting or staining artifacts, uneven staining, or background intensity were not considered for imaging. MNs <20 μm in diameter or displaying no VGluT1⁺ synapses were not included in the analysis. Cutting, immunostaining, and imaging was performed in batches that included samples from both genotypes; freshly cut and immunostained samples from the same WT mice were also routinely included and analyzed to ensure batch-to-batch reproducibility.

Image quantification was performed in ImageJ (National Institutes of Health). For the evaluation of the size of presynaptic terminals (VGluT1 and synaptophysin), three to five consecutive optical sections were collapsed in maximum-intensity projection, subjected to rolling-ball background subtraction, and thresholded for the segmentation of the synaptic terminals. The orientation of the synaptic structures (i.e., identification of the postsynaptic structures belonging to a selected MN) was

performed using cytoplasmic VAChT staining and the shape of the nucleus as references, as described above. The contour of the region of interest, including the area positive for VGluT1, synaptophysin, or bassoon, was traced manually in ImageJ, and the surface and mean intensity values were logged. For c-Fos quantification, the contour of the nucleus was delineated manually on maximum-intensity projections of confocal stacks, and the mean fluorescence intensity was logged.

Statistics
All values are provided as mean ± SD. Box-and-whiskers plots are defined such that the boxes extend from the lower to upper quartile values of the data, with a thick line at the median. The whiskers extend from the boxes up to the last point within the interval ±1.5× the interquartile range. Individual data points are overlaid on top of the boxes (note that, for the sake of clarity, at most 100 randomly chosen points are shown). *, $P < 0.05$; **, $P < 0.01$; ***, $P < 0.001$; and ****, $P < 0.0001$. Statistical tests were performed in Prism v.6.0.7 (GraphPad Software) and SciPy Python v.1.4.1 (Virtanen et al., 2020). Figures were generated using matplotlib v.3.1.3 (Hunter, 2007), seaborn v.0.10.0 (Waskom et al., 2020), and ImageJ v.2.0.0 (Schindelin et al., 2015).

Electrophysiology
Results obtained from wtSOD1 MNs were compared with the ones from mutSOD1 animals using appropriate statistical tests. The tests were chosen based on data distribution (Shapiro–Wilk normality test) and variance (F test). For data with normal distribution, we used Student's t test, and for data with nonnormal distribution, we used Wilcoxon–Mann–Whitney rank sum test. In all cases, the significance level was set at $P < 0.05$.

Synaptic coverage
For the synapses on the soma, the synaptic density was calculated as the number of VGluT1 appositions divided by the surface of the reconstructed 3D model of the MN soma using Neurolucida (number of synapses per 100 μm² of soma). For dendrite analysis, we considered dendrites to be proximal if (i) they were located in the section containing the soma, (ii) the path of the dendrite could be traced back to the soma, and (iii) the dendritic path length was <100 μm from the soma. Dendrites segments from at least two 50-μm-thick sections (>100-μm radial distance) away from the soma were considered as distal dendrites (spread in four to seven different spinal cord sections per animal). The density of synapses was computed for each dendritic segment (number of synapses per 100 μm). Differences were analyzed using Wilcoxon–Mann–Whitney rank sum test. The significance level was set at $P < 0.05$.

Synaptic proteins analysis
For the analysis of synaptic proteins, confocal stacks were manipulated in ImageJ; the same manipulations were applied to all images across replicates and genotypes. For fluorescence intensity quantification, small stacks (three to five optical sections) were collapsed in maximum-intensity projection, and on the resulting projected images, regions of interest were manually traced either overlapping the presynaptic marker or in the

volume adjacent to it (for the analysis of postsynaptic proteins). Each image was thresholded (different threshold for each synaptic protein; Roselli et al., 2009) to standardize the identification of pre- and postsynaptic clusters. For each presynaptic protein, the average fluorescence intensity value was obtained and individually plotted. For postsynaptic proteins, whenever multiple postsynaptic clusters were detected, they were measured separately, and the fluorescence intensity value was averaged. For determination of the cluster area, the cumulative area of GluR4 or Homer1b clusters was determined by measuring the area of individual clusters (after thresholding) and summing the area of all clusters corresponding to a given presynaptic terminal. Background fluorescence was measured locally and subtracted. Mann–Whitney nonparametric U tests (MW) were used to compare WT and mutSOD1 MNs. For chemogenetic experiments, one- or two-way ANOVAs, followed by Tukey honestly significant difference (HSD) tests, were used to test the effects of infection versus genotype. The significance level was set at $P < 0.05$.

Online supplemental material

Fig. S1 shows how EPSP grows with the stimulation intensity and that EPSP amplitude measurements are not distorted by disynaptic inhibition. It also shows that the level of presynaptic inhibition is similar in wtSOD1 and mutSOD1 mice. Fig. S2 shows that the presynaptic elements are not affected by the mutation. Fig. S3 shows that dendrites of mutSOD1 MNs become vacuolized, and that the size of the vacuoles increases with disease progression. Fig. S4 shows a representative image of a spinal cord after intraspinal injection of an AAV, illustrating the high rate of infection that can be achieved at the site of injection. In addition, the figure shows that increasing MN activity via act-PSAM restores the quantity of GluR4 and Homer1b proteins at VGluT1+ synapses. It also includes data demonstrating the specificity of the GluR4 antibody. Fig. S5 explains the method used for MLF stimulation and shows examples of atypical responses seen in a few MNs.

## References

Akay, T., W.G. Tourtellotte, S. Arber, and T.M. Jessell. 2014. Degradation of mouse locomotor pattern in the absence of proprioceptive sensory feedback. *Proc. Natl. Acad. Sci. USA.* 111:16877–16882. https://doi.org/10.1073/pnas.1419045111

Aldrin-Kirk, P., A. Heuer, G. Wang, B. Mattsson, M. Lundblad, M. Parmar, and T. Björklund. 2016. DREADD Modulation of Transplanted DA Neurons Reveals a Novel Parkinsonian Dyskinesia Mechanism Mediated by the Serotonin 5-HT6 Receptor. *Neuron.* 90:955–968. https://doi.org/10.1016/j.neuron.2016.04.017

Alstermark, B., and J. Ogawa. 2004. In vivo recordings of bulbospinal excitation in adult mouse forelimb motoneurons. *J. Neurophysiol.* 92: 1958–1962. https://doi.org/10.1152/jn.00092.2004

Alvarez, F.J., H.E. Titus-Mitchell, K.L. Bullinger, M. Kraszpulski, P. Nardelli, and T.C. Cope. 2011. Permanent central synaptic disconnection of proprioceptors after nerve injury and regeneration. I. Loss of VGLUT1/IA synapses on motoneurons. *J. Neurophysiol.* 106:2450–2470. https://doi.org/10.1152/jn.01095.2010

Babiec, W.E., R. Guglietta, and T.J. O'Dell. 2016. Basal levels of AMPA receptor GluA1 subunit phosphorylation at threonine 840 and serine 845 in hippocampal neurons. *Learn. Mem.* 23:127–133. https://doi.org/10.1101/lm.040675.115

Bading, H.. 2013. Nuclear calcium signalling in the regulation of brain function. *Nat. Rev. Neurosci.* 14:593–608. https://doi.org/10.1038/nrn3531

Bading, H.. 2017. Therapeutic targeting of the pathological triad of extrasynaptic NMDA receptor signaling in neurodegenerations. *J. Exp. Med.* 214:569–578. https://doi.org/10.1084/jem.20161673

Basaldella, E., A. Takeoka, M. Sigrist, and S. Arber. 2015. Multisensory Signaling Shapes Vestibulo-Motor Circuit Specificity. *Cell.* 163:301–312. https://doi.org/10.1016/j.cell.2015.09.023

Beyer, B., C. Deleuze, V.A. Letts, C.L. Mahaffey, R.M. Boumil, T.A. Lew, J.R. Huguenard, and W.N. Frankel. 2008. Absence seizures in C3H/HeJ and knockout mice caused by mutation of the AMPA receptor subunit Gria4. *Hum. Mol. Genet.* 17:1738–1749. https://doi.org/10.1093/hmg/ddn064

Binder, M.D., C.J. Heckman, and R.K. Powers. 1993. How different afferent inputs control motoneuron discharge and the output of the motoneuron pool. *Curr. Opin. Neurobiol.* 3:1028–1034. https://doi.org/10.1016/0959-4388(93)90177-Z

Carlsen, E.M., and J.-F. Perrier. 2014. Purines released from astrocytes inhibit excitatory synaptic transmission in the ventral horn of the spinal cord. *Front. Neural Circuits.* 8:60. https://doi.org/10.3389/fncir.2014.00060

Commisso, B., L. Ding, K. Varadi, M. Gorges, D. Bayer, T.M. Boeckers, A.C. Ludolph, J. Kassubek, O.J. Müller, and F. Roselli. 2018. Stage-dependent remodeling of projections to motor cortex in ALS mouse model revealed by a new variant retrograde-AAV9. *eLife.* 7. e36892. https://doi.org/10.7554/eLife.36892

Delestrée, N., M. Manuel, C. Iglesias, S.M. Elbasiouny, C.J. Heckman, and D. Zytnicki. 2014. Adult spinal motoneurones are not hyperexcitable in a mouse model of inherited amyotrophic lateral sclerosis. *J. Physiol.* 592:1687–1703. https://doi.org/10.1113/jphysiol.2013.265843

Delgado, J.Y., M. Coba, C.N.G. Anderson, K.R. Thompson, E.E. Gray, C.L. Heusner, K.C. Martin, S.G.N. Grant, and T.J. O'Dell. 2007. NMDA receptor activation dephosphorylates AMPA receptor glutamate receptor 1 subunits at threonine 840. *J. Neurosci.* 27:13210–13221. https://doi.org/10.1523/JNEUROSCI.3056-07.2007

Diering, G.H., A.S. Gustina, and R.L. Huganir. 2014. PKA-GluA1 coupling via AKAP5 controls AMPA receptor phosphorylation and cell-surface targeting during bidirectional homeostatic plasticity. *Neuron.* 84:790–805. https://doi.org/10.1016/j.neuron.2014.09.024

Eisen, A., H. Braak, K. Del Tredici, R. Lemon, A.C. Ludolph, and M.C. Kiernan. 2017. Cortical influences drive amyotrophic lateral sclerosis. *J. Neurol. Neurosurg. Psychiatry.* 88:917–924. https://doi.org/10.1136/jnnp-2017-315573

Esteban, J.A., S.-H. Shi, C. Wilson, M. Nuriya, R.L. Huganir, and R. Malinow. 2003. PKA phosphorylation of AMPA receptor subunits controls synaptic trafficking underlying plasticity. *Nat. Neurosci.* 6:136–143. https://doi.org/10.1038/nn997

Farrell, M.S., Y. Pei, Y. Wan, P.N. Yadav, T.L. Daigle, D.J. Urban, H.-M. Lee, N. Sciaky, A. Simmons, R.J. Nonneman, et al. 2013. A Gαs DREADD mouse for selective modulation of cAMP production in striatopallidal neurons. *Neuropsychopharmacology.* 38:854–862. https://doi.org/10.1038/npp.2012.251

Fink, A.J.P., K.R. Croce, Z.J. Huang, L.F. Abbott, T.M. Jessell, and E. Azim. 2014. Presynaptic inhibition of spinal sensory feedback ensures smooth movement. *Nature.* 509:43–48. https://doi.org/10.1038/nature13276

Fletcher, E.V., C.M. Simon, J.G. Pagiazitis, J.I. Chalif, A. Vukojicic, E. Drobac, X. Wang, and G.Z. Mentis. 2017. Reduced sensory synaptic excitation impairs motor neuron function via Kv2.1 in spinal muscular atrophy. *Nat. Neurosci.* 20:905–916. https://doi.org/10.1038/nn.4561

Franklin, K.B.J., and G. Paxinos. 2008. The Mouse Brain in Stereotaxic Coordinates 3. Elsevier, AP, Amsterdam.

Gomes, A.R., S.S. Correia, J.A. Esteban, C.B. Duarte, and A.L. Carvalho. 2007. PKC anchoring to GluR4 AMPA receptor subunit modulates PKC-driven receptor phosphorylation and surface expression. *Traffic.* 8:259–269. https://doi.org/10.1111/j.1600-0854.2006.00521.x

Gustafsson, B., and E. Jankowska. 1976. Direct and indirect activation of nerve cells by electrical pulses applied extracellularly. *J. Physiol.* 258:33–61. https://doi.org/10.1113/jphysiol.1976.sp011405

Hadano, S., A. Otomo, R. Kunita, K. Suzuki-Utsunomiya, A. Akatsuka, M. Koike, M. Aoki, Y. Uchiyama, Y. Itoyama, and J.-E. Ikeda. 2010. Loss of ALS2/Alsin exacerbates motor dysfunction in a SOD1-expressing mouse ALS model by disturbing endolysosomal trafficking. *PLoS One.* 5. e9805. https://doi.org/10.1371/journal.pone.0009805

Hardingham, G.E., S. Chawla, C.M. Johnson, and H. Bading. 1997. Distinct functions of nuclear and cytoplasmic calcium in the control of gene expression. *Nature.* 385:260–265. https://doi.org/10.1038/385260a0

Hedegaard, A., J. Lehnhoff, M. Moldovan, N.C. Petersen, and C.F. Meehan. 2015. Postactivation depression of the Ia EPSP in motoneurons is reduced in both the G127X SOD1 model of amyotrophic lateral sclerosis and in aged mice. *J. Neurophysiol.* 114:1196–1210. https://doi.org/10.1152/jn.00745.2014

Hultborn, H., M. Illert, J. Nielsen, A. Paul, M. Ballegaard, and H. Wiese. 1996. On the mechanism of the post-activation depression of the H-reflex in human subjects. *Exp. Brain Res.* 108:450–462. https://doi.org/10.1007/BF00227268

Hunter, J.D.. 2007. Matplotlib: A 2D Graphics Environment. *Comput. Sci. Eng.* 9:90–95. https://doi.org/10.1109/MCSE.2007.55

Imlach, W.L., E.S. Beck, B.J. Choi, F. Lotti, L. Pellizzoni, and B.D. McCabe. 2012. SMN is required for sensory-motor circuit function in Drosophila. *Cell.* 151:427–439. https://doi.org/10.1016/j.cell.2012.09.011

Jenkins, M.A., G. Wells, J. Bachman, J.P. Snyder, A. Jenkins, R.L. Huganir, R.E. Oswald, and S.F. Traynelis. 2014. Regulation of GluA1 α-amino-3-hydroxy-5-methyl-4-isoxazolepropionic acid receptor function by protein kinase C at serine-818 and threonine-840. *Mol. Pharmacol.* 85:618–629. https://doi.org/10.1124/mol.113.091488

Kim, J., E.G. Hughes, A.S. Shetty, P. Arlotta, L.A. Goff, D.E. Bergles, and S.P. Brown. 2017. Changes in the Excitability of Neocortical Neurons in a Mouse Model of Amyotrophic Lateral Sclerosis Are Not Specific to Corticospinal Neurons and Are Modulated by Advancing Disease. *J. Neurosci.* 37:9037–9053. https://doi.org/10.1523/JNEUROSCI.0811-17.2017

Lacar, B., S.B. Linker, B.N. Jaeger, S.R. Krishnaswami, J.J. Barron, M.J.E. Kelder, S.L. Parylak, A.C.M. Paquola, P. Venepally, M. Novotny, et al. 2016. Nuclear RNA-seq of single neurons reveals molecular signatures of activation. *Nat. Commun.* 7:11022. https://doi.org/10.1038/ncomms11022

Lalancette-Hebert, M., A. Sharma, A.K. Lyashchenko, and N.A. Shneider. 2016. Gamma motor neurons survive and exacerbate alpha motor neuron degeneration in ALS. *Proc. Natl. Acad. Sci. USA.* 113:E8316–E8325. https://doi.org/10.1073/pnas.1605210113

Lalley, P.M., O. Pierrefiche, A.M. Bischoff, and D.W. Richter. 1997. cAMP-dependent protein kinase modulates expiratory neurons in vivo. *J. Neurophysiol.* 77:1119–1131. https://doi.org/10.1152/jn.1997.77.3.1119

Le Masson, G., S. Przedborski, and L.F. Abbott. 2014. A computational model of motor neuron degeneration. *Neuron.* 83:975–988. https://doi.org/10.1016/j.neuron.2014.07.001

Leroy, F., B. Lamotte d'Incamps, R.D. Imhoff-Manuel, and D. Zytnicki. 2014. Early intrinsic hyperexcitability does not contribute to motoneuron degeneration in amyotrophic lateral sclerosis. *eLife.* 3. e04046. https://doi.org/10.7554/eLife.04046

Liang, H., T. Bácskai, C. Watson, and G. Paxinos. 2014. Projections from the lateral vestibular nucleus to the spinal cord in the mouse. *Brain Struct. Funct.* 219:805–815. https://doi.org/10.1007/s00429-013-0536-4

Lokireddy, S., N.V. Kukushkin, and A.L. Goldberg. 2015. cAMP-induced phosphorylation of 26S proteasomes on Rpn6/PSMD11 enhances their activity and the degradation of misfolded proteins. *Proc. Natl. Acad. Sci. USA.* 112:E7176–E7185. https://doi.org/10.1073/pnas.1522332112

Lu, Y., X.M. Zha, E.Y. Kim, S. Schachtele, M.E. Dailey, D.D. Hall, S. Strack, S.H. Green, D.A. Hoffman, and J.W. Hell. 2011. A kinase anchor protein 150 (AKAP150)-associated protein kinase A limits dendritic spine density. *J. Biol. Chem.* 286:26496–26506. https://doi.org/10.1074/jbc.M111.254912

Magnus, C.J., P.H. Lee, D. Atasoy, H.H. Su, L.L. Looger, and S.M. Sternson. 2011. Chemical and genetic engineering of selective ion channel-ligand interactions. *Science.* 333:1292–1296. https://doi.org/10.1126/science.1206606

Manuel, M., C. Iglesias, M. Donnet, F. Leroy, C.J. Heckman, and D. Zytnicki. 2009. Fast kinetics, high-frequency oscillations, and subprimary firing range in adult mouse spinal motoneurons. *J. Neurosci.* 29:11246–11256. https://doi.org/10.1523/JNEUROSCI.3260-09.2009

Manuel, M., C. Meunier, M. Donnet, and D. Zytnicki. 2007. Resonant or not, two amplification modes of proprioceptive inputs by persistent inward currents in spinal motoneurons. *J. Neurosci.* 27:12977–12988. https://doi.org/10.1523/JNEUROSCI.3299-07.2007

Martínez-Silva, M.L., R.D. Imhoff-Manuel, A. Sharma, C.J. Heckman, N.A. Shneider, F. Roselli, D. Zytnicki, and M. Manuel. 2018. Hypoexcitability precedes denervation in the large fast-contracting motor units in two unrelated mouse models of ALS. *eLife.* 7. e30955. https://doi.org/10.7554/eLife.30955

Mentis, G.Z., D. Blivis, W. Liu, E. Drobac, M.E. Crowder, L. Kong, F.J. Alvarez, C.J. Sumner, and M.J. O'Donovan. 2011. Early functional impairment of sensory-motor connectivity in a mouse model of spinal muscular atrophy. *Neuron.* 69:453–467. https://doi.org/10.1016/j.neuron.2010.12.032

O'Brien, R.J., S. Kamboj, M.D. Ehlers, K.R. Rosen, G.D. Fischbach, and R.L. Huganir. 1998. Activity-dependent modulation of synaptic AMPA receptor accumulation. *Neuron.* 21:1067–1078. https://doi.org/10.1016/S0896-6273(00)80624-8

Ouali Alami, N., C. Schurr, F. Olde Heuvel, L. Tang, Q. Li, A. Tasdogan, A. Kimbara, M. Nettekoven, G. Ottaviani, C. Raposo, et al. 2018. NF-κB activation in astrocytes drives a stage-specific beneficial neuro-immunological response in ALS. *EMBO J.* 37. e98697. https://doi.org/10.15252/embj.201798697

Peter, S., M.M. Ten Brinke, J. Stedehouder, C.M. Reinelt, B. Wu, H. Zhou, K. Zhou, H.-J. Boele, S.A. Kushner, M.G. Lee, et al. 2016. Dysfunctional

cerebellar Purkinje cells contribute to autism-like behaviour in Shank2-deficient mice. *Nat. Commun.* 7:12627. https://doi.org/10.1038/ncomms12627

Petrov, D., C. Mansfield, A. Moussy, and O. Hermine. 2017. ALS Clinical Trials Review: 20 Years of Failure. Are We Any Closer to Registering a New Treatment? *Front. Aging Neurosci.* 9:68. https://doi.org/10.3389/fnagi.2017.00068

Pieri, M., F. Albo, C. Gaetti, A. Spalloni, C.P. Bengtson, P. Longone, S. Cavalcanti, and C. Zona. 2003. Altered excitability of motor neurons in a transgenic mouse model of familial amyotrophic lateral sclerosis. *Neurosci. Lett.* 351:153–156. https://doi.org/10.1016/j.neulet.2003.07.010

Pun, S., A.F. Santos, S. Saxena, L. Xu, and P. Caroni. 2006. Selective vulnerability and pruning of phasic motoneuron axons in motoneuron disease alleviated by CNTF. *Nat. Neurosci.* 9:408–419. https://doi.org/10.1038/nn1653

Quinlan, K.A., E. Kajtaz, J.D. Ciolino, R.D. Imhoff-Manuel, M.C. Tresch, C.J. Heckman, and V.M. Tysseling. 2017. Chronic electromyograms in treadmill running SOD1 mice reveal early changes in muscle activation. *J. Physiol.* 595:5387–5400. https://doi.org/10.1113/JP274170

Ragnarson, B., G. Ornung, G. Grant, O.P. Ottersen, and B. Ulfhake. 2003. Glutamate and AMPA receptor immunoreactivity in Ia synapses with motoneurons and neurons of the central cervical nucleus. *Exp. Brain Res.* 149:447–457. https://doi.org/10.1007/s00221-003-1388-6

Roselli, F., and P. Caroni. 2015. From intrinsic firing properties to selective neuronal vulnerability in neurodegenerative diseases. *Neuron.* 85:901–910. https://doi.org/10.1016/j.neuron.2014.12.063

Roselli, F., P. Hutzler, Y. Wegerich, P. Livrea, and O.F.X. Almeida. 2009. Disassembly of shank and homer synaptic clusters is driven by soluble beta-amyloid(1-40) through divergent NMDAR-dependent signalling pathways. *PLoS One.* 4. e6011. https://doi.org/10.1371/journal.pone.0006011

Roth, B.L.. 2016. DREADDs for Neuroscientists. *Neuron.* 89:683–694. https://doi.org/10.1016/j.neuron.2016.01.040

Rothstein, J.D.. 2009. Current hypotheses for the underlying biology of amyotrophic lateral sclerosis. *Ann. Neurol.* 65(S1, Suppl 1):S3–S9. https://doi.org/10.1002/ana.21543

Rothstein, J.D., G. Tsai, R.W. Kuncl, L. Clawson, D.R. Cornblath, D.B. Drachman, A. Pestronk, B.L. Stauch, and J.T. Coyle. 1990. Abnormal excitatory amino acid metabolism in amyotrophic lateral sclerosis. *Ann. Neurol.* 28:18–25. https://doi.org/10.1002/ana.410280106

Rotterman, T.M., P. Nardelli, T.C. Cope, and F.J. Alvarez. 2014. Normal distribution of VGLUT1 synapses on spinal motoneuron dendrites and their reorganization after nerve injury. *J. Neurosci.* 34:3475–3492. https://doi.org/10.1523/JNEUROSCI.4768-13.2014

Rudnick, N.D., C.J. Griffey, P. Guarnieri, V. Gerbino, X. Wang, J.A. Piersaint, J.C. Tapia, M.M. Rich, and T. Maniatis. 2017. Distinct roles for motor neuron autophagy early and late in the SOD1^{G93A} mouse model of ALS. *Proc. Natl. Acad. Sci. USA.* 114:E8294–E8303. https://doi.org/10.1073/pnas.1704294114

Rudomin, P., and R.F. Schmidt. 1999. Presynaptic inhibition in the vertebrate spinal cord revisited. *Exp. Brain Res.* 129:1–37. https://doi.org/10.1007/s002210050933

Ruediger, S., C. Vittori, E. Bednarek, C. Genoud, P. Strata, B. Sacchetti, and P. Caroni. 2011. Learning-related feedforward inhibitory connectivity growth required for memory precision. *Nature.* 473:514–518. https://doi.org/10.1038/nature09946

Ruegsegger, C., D.M. Stucki, S. Steiner, N. Angliker, J. Radecke, E. Keller, B. Zuber, M.A. Rüegg, and S. Saxena. 2016. Impaired mTORC1-Dependent Expression of Homer-3 Influences SCA1 Pathophysiology. *Neuron.* 89:129–146. https://doi.org/10.1016/j.neuron.2015.11.033

Saba, L., M.T. Viscomi, S. Caioli, A. Pignataro, E. Bisicchia, M. Pieri, M. Molinari, M. Ammassari-Teule, and C. Zona. 2016. Altered Functionality, Morphology, and Vesicular Glutamate Transporter Expression of Cortical Motor Neurons from a Presymptomatic Mouse Model of Amyotrophic Lateral Sclerosis. *Cereb. Cortex.* 26:1512–1528. https://doi.org/10.1093/cercor/bhu317

Saxena, S., F. Roselli, K. Singh, K. Leptien, J.P. Julien, F. Gros-Louis, and P. Caroni. 2013. Neuroprotection through excitability and mTOR required in ALS motoneurons to delay disease and extend survival. *Neuron.* 80:80–96. https://doi.org/10.1016/j.neuron.2013.07.027

Schindelin, J., C.T. Rueden, M.C. Hiner, and K.W. Eliceiri. 2015. The ImageJ ecosystem: An open platform for biomedical image analysis. *Mol. Reprod. Dev.* 82:518–529. https://doi.org/10.1002/mrd.22489

Seok, S., T. Fu, S.-E. Choi, Y. Li, R. Zhu, S. Kumar, X. Sun, G. Yoon, Y. Kang, W. Zhong, et al. 2014. Transcriptional regulation of autophagy by an FXR-CREB axis. *Nature.* 516:108–111. https://doi.org/10.1038/nature13949

Sheng, M., and C.C. Hoogenraad. 2007. The postsynaptic architecture of excitatory synapses: a more quantitative view. *Annu. Rev. Biochem.* 76:823–847. https://doi.org/10.1146/annurev.biochem.76.060805.160029

Shiraishi, Y., A. Mizutani, K. Mikoshiba, and T. Furuichi. 2003. Coincidence in dendritic clustering and synaptic targeting of homer proteins and NMDA receptor complex proteins NR2B and PSD95 during development of cultured hippocampal neurons. *Mol. Cell. Neurosci.* 22:188–201. https://doi.org/10.1016/S1044-7431(03)00037-X

Soo, K.Y., M. Halloran, V. Sundaramoorthy, S. Parakh, R.P. Toth, K.A. Southam, C.A. McLean, P. Lock, A. King, M.A. Farg, et al. 2015. Rab1-dependent ER-Golgi transport dysfunction is a common pathogenic mechanism in SOD1, TDP-43 and FUS-associated ALS. *Acta Neuropathol.* 130:679–697. https://doi.org/10.1007/s00401-015-1468-2

States, B.A., L. Khatri, and E.B. Ziff. 2008. Stable synaptic retention of serine-880-phosphorylated GluR2 in hippocampal neurons. *Mol. Cell. Neurosci.* 38:189–202. https://doi.org/10.1016/j.mcn.2008.02.003

Stuart, G.J., and S.J. Redman. 1991. Mechanisms of presynaptic inhibition studied using paired-pulse facilitation. *Neurosci. Lett.* 126:179–183. https://doi.org/10.1016/0304-3940(91)90548-8

Turrigiano, G.G., K.R. Leslie, N.S. Desai, L.C. Rutherford, and S.B. Nelson. 1998. Activity-dependent scaling of quantal amplitude in neocortical neurons. *Nature.* 391:892–896. https://doi.org/10.1038/36103

van Dis, V., M. Kuijpers, E.D. Haasdijk, E. Teuling, S.A. Oakes, C.C. Hoogenraad, and D. Jaarsma. 2014. Golgi fragmentation precedes neuromuscular denervation and is associated with endosome abnormalities in SOD1-ALS mouse motor neurons. *Acta Neuropathol. Commun.* 2:38. https://doi.org/10.1186/2051-5960-2-38

Vaughan, S.K., Z. Kemp, T. Hatzipetros, F. Vieira, and G. Valdez. 2015. Degeneration of proprioceptive sensory nerve endings in mice harboring amyotrophic lateral sclerosis-causing mutations. *J. Comp. Neurol.* 523:2477–2494. https://doi.org/10.1002/cne.23848

VerPlank, J.J.S., S. Lokireddy, J. Zhao, and A.L. Goldberg. 2019. 26S Proteasomes are rapidly activated by diverse hormones and physiological states that raise cAMP and cause Rpn6 phosphorylation. *Proc. Natl. Acad. Sci. USA.* 116:4228–4237. https://doi.org/10.1073/pnas.1809254116

Virtanen, P., R. Gommers, T.E. Oliphant, M. Haberland, T. Reddy, D. Cournapeau, E. Burovski, P. Peterson, W. Weckesser, J. Bright, et al; SciPy 1.0 Contributors. 2020. SciPy 1.0: fundamental algorithms for scientific computing in Python. *Nat. Methods.* 17:261–272. https://doi.org/10.1038/s41592-019-0686-2

von Lewinski, F., and B.U. Keller. 2005. Ca2+, mitochondria and selective motoneuron vulnerability: implications for ALS. *Trends Neurosci.* 28:494–500. https://doi.org/10.1016/j.tins.2005.07.001

Vucic, S., and M.C. Kiernan. 2006. Novel threshold tracking techniques suggest that cortical hyperexcitability is an early feature of motor neuron disease. *Brain.* 129:2436–2446. https://doi.org/10.1093/brain/awl172

Wang, J.-D., Y.-L. Cao, Q. Li, Y.-P. Yang, M. Jin, D. Chen, F. Wang, G.-H. Wang, Z.-H. Qin, L.-F. Hu, et al. 2015. A pivotal role of FOS-mediated BECN1/Beclin 1 upregulation in dopamine D2 and D3 receptor agonist-induced autophagy activation. *Autophagy.* 11:2057–2073. https://doi.org/10.1080/15548627.2015.1100930

Waskom, M., O. Botvinnik, J. Ostblom, S. Lukauskas, P. Hobson, M. Gelbart, D.C. Gemperline, T. Augspurger, Y. Halchenko, J.B. Cole, et al. 2020. mwaskom/seaborn: v0.10.0. Zenodo. Available at: https://doi.org/10.5281/zenodo.3629446.

Williams, T.L., P.G. Ince, A.E. Oakley, and P.J. Shaw. 1996. An immunocytochemical study of the distribution of AMPA selective glutamate receptor subunits in the normal human motor system. *Neuroscience.* 74:185–198. https://doi.org/10.1016/0306-4522(96)00117-0

Supplemental material
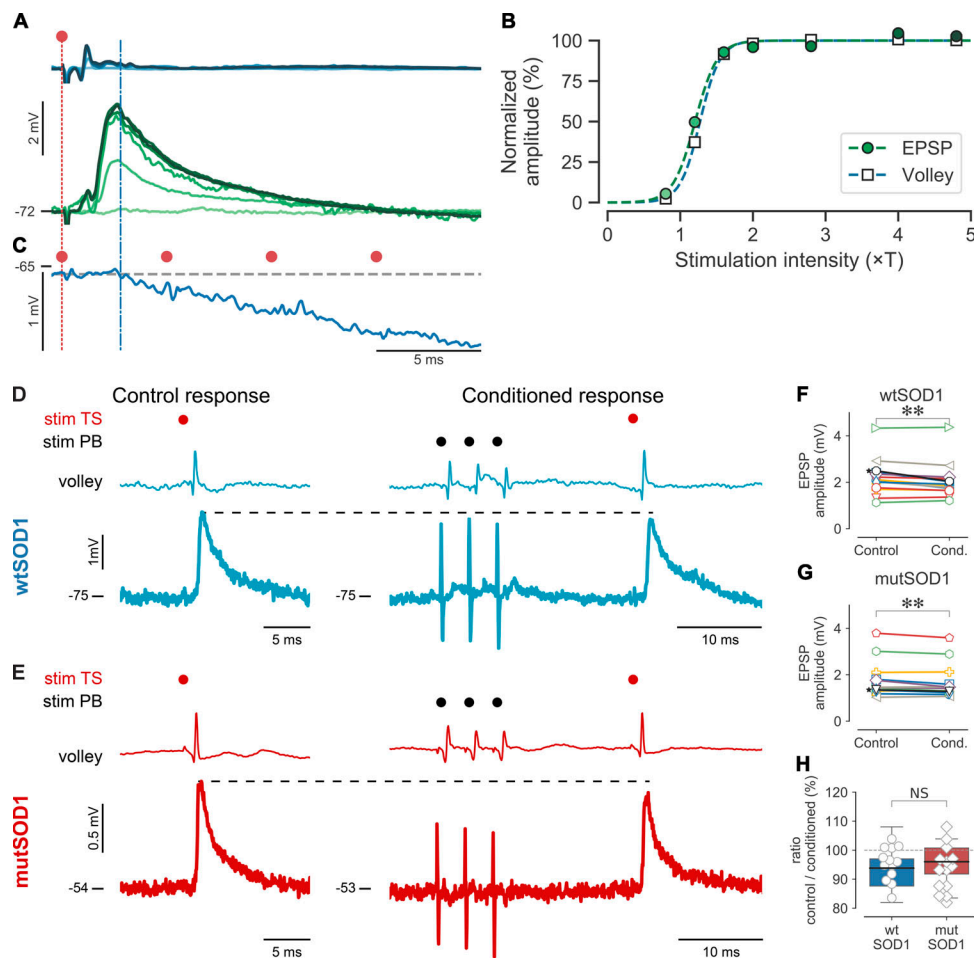
Figure S1. Inputs to TS MNs and presynaptic inhibition of Ia terminals. (A) Recordings from a mutSOD1 MN following nerve stimulation at different intensities normalized to the threshold intensity for the afferent volley. The stimulation was gradually increased up to 5× threshold. Top blue traces: Afferent volley recorded on the dorsal surface of the spinal cord. Bottom green traces: Membrane potential of the MN. The red dot designates the stimulation time. Stimulation artifacts were truncated. The central latency between the volley and the EPSP onset is <0.5 ms, indicating that the EPSP is monosynaptic. **(B)** Quantification of the amplitude of the EPSP measured at the peak (green dots and curve) and the peak-to-peak amplitude of the volley (unfilled squares and curve), showing that both reach a maximum at ~2× threshold intensity. At higher stimulation intensities, the amplitude plateaus, and we did not observe disynaptic EPSPs despite the possible recruitment of group II afferents. **(C)** Recording of Renshaw inhibition in a separate experiment, showing that disynaptic inhibition (vertical blue dotted line) arrives at longer latency than the peak of the monosynaptic EPSP. The motor axons in the nerve (L3–L5 dorsal roots cut) were stimulated at 200 Hz (red dots) to elicit a visible Renshaw inhibition through temporal facilitation. Note that it was not possible to isolate Ib inhibition or group II inhibition from Ia excitation, but these inhibitions are disynaptic and thus cannot occur faster than Renshaw inhibition. Therefore, the peak measurement of the monosynaptic EPSP is not contaminated by any inhibition. **(D–H)** Presynaptic inhibition in mouse MNs. We investigated whether Ia terminals from the TS are subject to presynaptic inhibition following a conditioning stimulation of group I afferents from posterior biceps (PB), i.e., the most classic pathway for presynaptic inhibition (Rudomin and Schmidt, 1999). **(D)** The left panel shows the unconditioned Ia monosynaptic EPSP on a wtSOD1 TS MN; the right panel shows the same Ia EPSP conditioned by group I afferents from the PB. The conditioning stimulation (black dots) is a train of three electric stimulations at 200 Hz that precedes the stimulation of the TS (red dots) by 23 ms. The conditioning stimulation reduces the test EPSP. We repeated this experiment in 14 wtSOD1 MNs (F) in which the conditioning stimulation elicited an average reduction of the test Ia EPSP of 6 ± 8%; paired *t* test, **, P = 0.004. Asterisk, example in D. **(E)** Presynaptic inhibition in a mutSOD1 MNs. Same arrangement as in D. We repeated this experiment in 13 mutSOD1 MNs (G) on which the conditioning stimulation elicited an average reduction of the test Ia EPSP of 5 ± 6%; paired *t* test, **, P = 0.006. Asterisk, example in E. **(H)** The effect of the conditioning stimulation on the size of Ia EPSPs was the same in wtSOD1 and mutSOD1 MNs (*t* test, P = 0.50), indicating that the strength of presynaptic inhibition is similar in the two phenotypes. Experiments were performed in four wtSOD1 mice and six mutSOD1 mice.
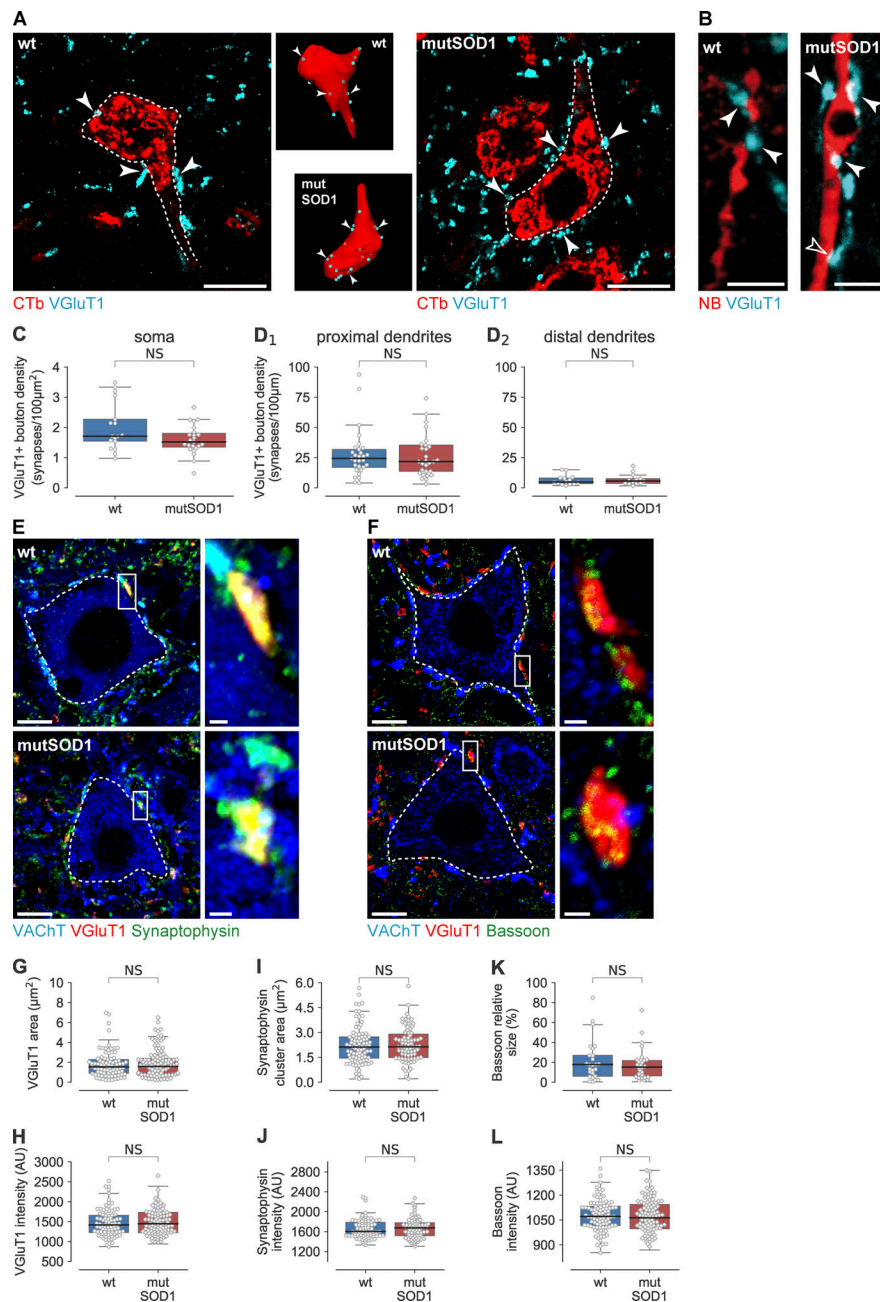
Figure S2. **No change in the presynaptic structure of VGluT1+ synapses onto MNs. (A)** Examples of immunolabeled VGluT1+ synapses juxtaposed to the soma of a WT and a mutSOD1 TS MN labeled with cholera toxin b (CTb). Scale bar: 20 µm. Insets show a 3D reconstruction of the cell soma with the location of the VGluT1+ boutons in blue. Arrowheads point to synapses visible in the optical plane of the corresponding example. **(B)** Immunolabeled VGluT1+ synapses on proximal dendritic segments of a WT and a mutSOD1 Neurobiotin-filled (NB) MN. Filled arrowheads point to VGluT1+ synapses on dendritic varicosities (vacuolized in the case of the mutSOD1 MN). The unfilled arrowhead points to a synapse at a distance from the vacuole. Scale bars: 5 µm. **(C)** Estimation of the synaptic density of VGluT1+ boutons on the soma. WT: 1.6 ± 0.5 synapses/100 µm², n = 23 (three mice); vs. mutSOD1 2.0 ± 0.8 synapses/100 µm²; n = 17 (three mice); MW, P = 0.18. **(D₁)** Estimation of the density of VGluT1+ boutons on proximal dendrites. WT: 28 ± 20 synapse/100 µm, n = 29 (four mice); vs. mutSOD1: 29 ± 23 synapse/100 µm, n = 29 (four mice); MW, P = 0.85. **(D₂)** Estimation of the density of VGluT1+ boutons on distal dendrites. WT: 6 ± 4 synapse/100 µm, n = 14 (four mice); vs. mutSOD1: 7 ± 5 synapse/100 µm, n = 13 (four mice); MW, P = 0.90. **(E)** Synaptophysin labeling in VGluT1+ synapses juxtaposed to a MN identified by VAChT labeling. Dotted line represents the approximate outline of the MN. Note that the intensity of the VAChT signal was intentionally boosted to highlight the presence of an intracellular signal in addition to the presence of the C-boutons to identify MNs. **(F)** Bassoon labeling. Scale bars: 10 µm (inset: 1 µm). **(G and H)** No difference in cluster area of VGluT1 (WT: 1.85 ± 1.41 µm², n = 179; vs. mutSOD1: 1.90 ± 1.36 µm², n = 202; MW, P = 0.73) or in VGluT1 fluorescence intensity in WT and mutSOD MNs (WT: 1,459 ± 315, n = 179; vs. mutSOD1: 1,494 ± 350, n = 202; MW, P = 0.45). **(I and J)** No difference in cluster size of synaptophysin (WT: 2.22 ± 1.13 µm², n = 91; vs. mutSOD1: 2.28 ± 1.04 µm², n = 75; MW, P = 0.55) or synaptophysin immunostaining intensity (WT: 1,653 ± 190, n = 91; vs. mutSOD1: 1,669 ± 203, n = 75; MW, P = 0.61) inside VGluT1+ synapses. **(K and L)** No difference in the size of bassoon puncta relative to the size of the VGluT1+ bouton (WT: 24 ± 26%, n = 36; vs. mutSOD1: 17 ± 14%, n = 37; MW, P = 0.44) or bassoon puncta immunostaining intensity (WT: 1073 ± 97, n = 118; vs. mutSOD1: 1,072 ± 103, n = 118; MW, P = 0.68) in WT and mutSOD MNs. Each point on the graphs represents one synapse. Experiments in EL were conducted on four WT and four mutSOD1 mice.
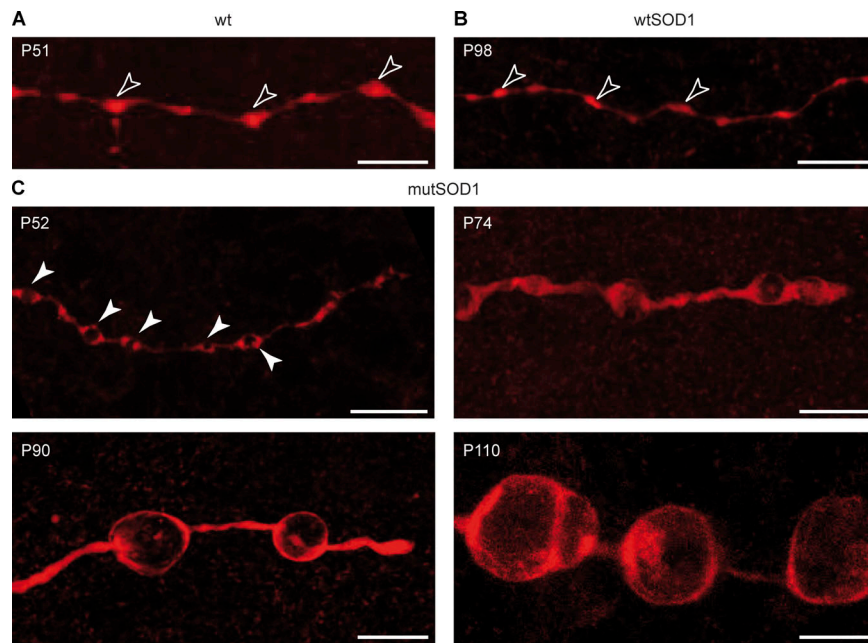
Figure S3. **MN dendrites of mutSOD1 animals display age-dependent vacuolization. (A)** Dendritic varicosities (unfilled arrowheads) in a WT MN at P51. **(B)** Dendritic varicosities (unfilled arrowheads) in a wtSOD1 MN at P98. **(C)** In mutSOD1 MNs, many varicosities display vacuoles (filled arrowheads). In contrast, dendritic varicosities do not display any vacuole in wtSOD1 MNs (B), indicating that the vacuoles do not result from the transgenes by themselves but are the consequence of the mutation. In mutSOD1 MNs, the vacuoles increase in size over time (C). Scale bars: 10 µm.
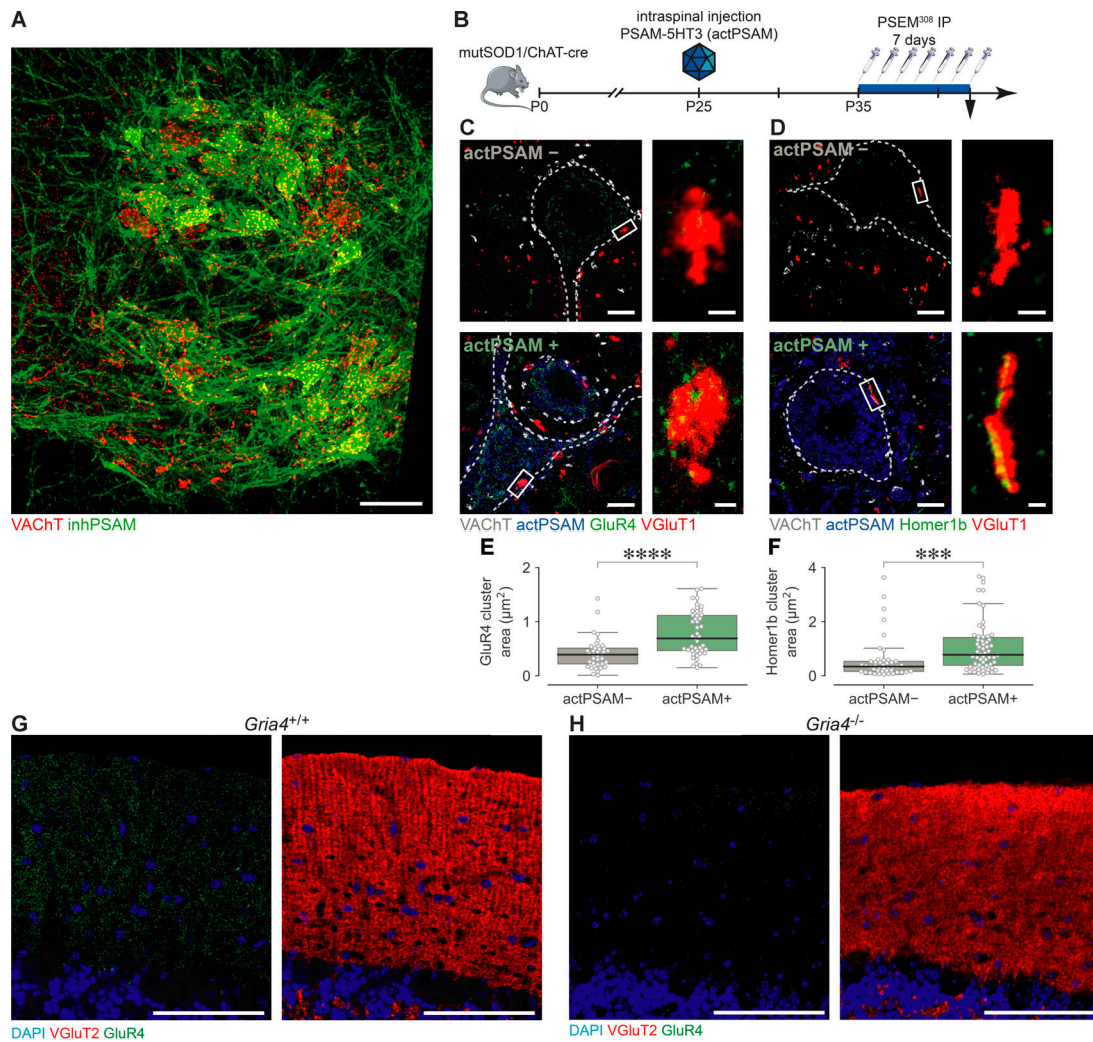
Figure S4. **Chemogenetic excitation of MNs rescues synaptic structure. (A)** Image of the ventral spinal cord of a mouse injected intraspinally with an AA9 expressing inhPSAM. This section was very close to the injection site, and the infection rate was very high there, as shown by the fact that very few MNs (identified by VAChT labeling, red) did not express inhPSAM (green). Scale bar: 50 µm. **(B)** Timeline for the unilateral intraspinal injection of AAV9 5HT3-PSAM (actPSAM) in double transgenic mutSOD1/ChAT-cre mice followed by injection of the specific ligand PSEM[308]. **(C and D)** GluR4 (C) and Homer1b (D) immunolabeling either in noninfected MNs (actPSAM⁻) or MNs expressing actPSAM (actPSAM⁺). The inset on the right is an enlargement of the region indicated with a white rectangle. In all panels, dotted lines represent the approximate outline of the MNs. Scale bar: 10 µm (inset: 1 µm). **(E)** Quantification of GluR4 cluster area at VGluT1⁺ synapses in actPSAM infected MN (actPSAM⁺) versus contralateral noninfected MN (actPSAM⁻). ActPSAM⁻ MNs: 0.4 ± 0.3 µm², $n = 37$; vs. actPSAM⁺ MNs: 0.8 ± 0.4 µm², $n = 47$; MW, ****, $P < 0.0001$. **(F)** Quantification of Homer1b cluster area at VGluT1⁺ synapses in actPSAM-infected MNs (actPSAM⁺) versus contralateral noninfected MNs (actPSAM⁻). actPSAM⁻ MNs: 0.6 ± 0.8 µm², $n = 44$; vs. actPSAM⁺ MNs: 1.1 ± 0.9 µm², $n = 62$; MW, ***, $P = 0.0002$. Each point on the graphs represents one synapse. **(G and H)** The specificity of the GluR4 antibody is demonstrated on the cerebellum of WT (G) and *Gria4* knockout (H) animals. Note the dense GluR4 labeling (green) in the molecular layer of WT animals while the labeling is almost completely absent in *Gria4⁻/⁻* animals despite the dense VGluT2 labeling (red). Scale bars: 100 µm.
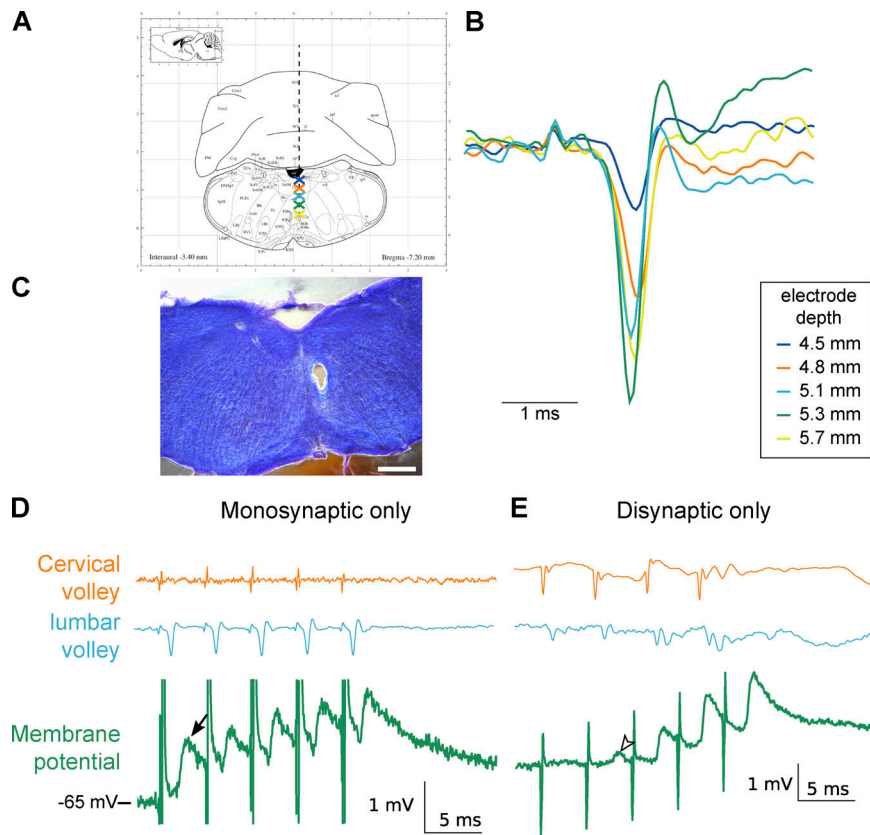
Figure S5. **Methodological considerations for MLF-evoked EPSP measurements. (A)** Representation of the path of the stimulation electrode (dashed line) in stereotaxic coordinates (adapted from Franklin and Paxinos, 2008). **(B)** Recordings of the lumbar volley produced by a single shock stimulation at 25 µA at each of the depths represented by a cross in A. The electrode was placed where the amplitude of the volley was maximal (in this case, 5.3 mm). **(C)** At the end of the experiment, an electrolytic lesion was performed at the location of the stimulation electrode to confirm correct placement. Scale bar: 0.5 mm. **(D)** Example of recording in which only monosynaptic EPSPs were visible (filled arrow). Note the lack of disynaptic EPSP "bump" on the response to the last stimulation. **(E)** Example of recording in which only disynaptic excitation (unfilled arrowhead) was visible. In this cell, the stimulation of descending fibers did not evoke monosynaptic EPSP, indicating that they did not project directly to this MN. The disynaptic EPSP started to appear in response to the second stimulation (unfilled arrowhead) and grew upon stimulation repetition, indicating temporal summation of the excitatory interneurons activated by the descending fibers. The latency of disynaptic response is ~1 ms longer than for the monosynaptic response. Note that because this MN did not display any monosynaptic component, it was not included in our analysis.